

Numerical convergence of physical variables in hydrodynamical simulations of cooling clusters

R. Valdarnini¹

SISSA Via Beirut 2-4 34014, Trieste, Italy

valda@sissa.it

ABSTRACT

Results from hydrodynamical SPH simulations of galaxy clusters are used to investigate the dependence of the final cluster X-ray properties on the numerical resolution and the assumed models for the physical gas processes. Two different spatially flat cosmological models have been considered: a low-density cold dark matter universe with a vacuum energy density $\Omega_\Lambda = 0.7$ (Λ CDM) and a cold+hot dark matter model (CHDM). For each of these models two different clusters have been extracted from a cosmological N -body simulation. A series of hydrodynamical simulations has then been performed for each of them using a TREE-SPH code. These simulations first include radiative cooling and then also conversion of cold gas particles into stars; because of supernova explosions these particles can release energy in the form of thermal energy to the surrounding intracluster gas. For a specific treatment for the thermal state of the gas, simulation runs have been performed with different numerical resolutions. This is in order to disentangle in the final results for the cluster profiles, the effects of the resolution from those due to the assumed model for the gas thermal evolution. The numerical resolution of the simulation is controlled by the number of gas particles N_g and the chosen value for the gas gravitational softening parameter ε_g . The latter is proportional to the minimum SPH smoothing length and therefore sets a maximum spatial resolution for the simulations. For the cooling runs, final X-ray luminosities have been found to be diverging according to $L_X \propto 1/\varepsilon_g^5$. The gas density profiles are also diverging at the cluster center. This is in agreement with previous findings. When cold gas particles are allowed to convert into stars, the divergences are removed. The final gas profiles show a well defined core radius and the temperature profiles are nearly flat. For the most massive test cluster in the Λ CDM model, these simulations show a prominent cooling flow in the cluster core. This cluster was analyzed in detail, running simulations with different star formation methods and increasing numerical resolution. A

comparison between different runs shows that the results of simulations, based on star formation methods in which gas conversion into stars is controlled by an efficiency parameter c_* , are sensitive to the numerical resolution of the simulation. In this respect star formation methods based instead on a local density threshold, as in Navarro and White (1993), are shown to give more stable results. Final X-ray luminosities are found to be numerically stable, with uncertainties of a factor ~ 2 . These simulations are also in good agreement with observational data when the final results are compared with the observed star formation rate and the luminosity-temperature relation from cooling flow clusters. Therefore I find that hydrodynamical simulations of cooling clusters can be used to give reliably predictions of the cluster X-ray properties. For a given numerical resolution, the conversion of cool gas particles into stars as in Navarro and White should be preferred.

Subject headings: cosmology: clusters–galaxies:clusters–methods:numerical

1. Introduction

Galaxy clusters are the largest virialized structures known in the universe. According to the hierarchical scenario their evolution rate is a strong function of the background cosmology (Peebles, Daly & Juszkievicz 1989; Lilje 1992; Viana & Liddle 1999; Oukbir & Blanchard 1992; Eke et al. 1998; Sadat, Blanchard & Oukbir 1998; Bahcall, Fan & Cen 1997), thus making galaxy clusters natural tools for constraining the cosmological models. Galaxy clusters are also powerful X-ray emitters. X-ray observations have shown that most of the baryons in galaxy clusters are in the form of hot ($T \simeq 10^7 K$) ionized X-ray emitting gas (Forman & Jones 1982; Sarazin 1986). The bulk of the emission is via thermal bremsstrahlung; its dependence on the square of the gas density allows one to select cluster samples without the contamination effects which may arise in the optical band. For this reason, galaxy clusters have been the subject of extensive observational programs in the X-ray band (Henry et al. 1992; Henry 1997; Ebeling et al. 1997; Rosati et al. 1998). Observations of the cluster X-ray emission and temperature can be used to reconstruct the radial gas density and temperature profile, assuming spherical symmetry. The gas density profile has a radial fall-off with slope $\simeq -2$ and a constant density core in the inner regions, with typical size $r_g \simeq 50 - 200 h^{-1} Kpc$ (Sarazin 1986); the gas temperature profile is instead nearly isothermal within the virial radius. The density of the gas can be used to recover the dark matter profile and the total cluster mass. Assuming virial equilibrium these cluster properties are connected to the primeval power spectrum and the assumed cosmological

model, thus providing important clues for testing cosmologies (Makino, Sasaki & Suto 1998; Navarro, Frenk & White 1997).

Other cosmological information can be obtained from the statistical properties of the ensemble of X-ray clusters. X-ray observations of cluster number counts, the X-ray temperature function (Henry & Arnoud 1991; Edge et al. 1990; Henry 1997) and the X-ray luminosity function (Rosati et al. 1998; Ebeling et al. 1998) are powerful probes for constraining the values of the cosmological parameters Ω_0 and σ_8 (Henry & Arnoud 1991; White, Efstathiou & Frenk 1993; Bahcall & Fan 1998; Eke, Cole & Frenk 1996; Kitayama, Sasaki & Suto 1998). An analytical framework for connecting the X-ray temperature and the luminosity function to theoretical models can be obtained, within the Press & Schechter (1974) approach, by assuming hydrostatic equilibrium for the gas distribution and neglecting radiative cooling. In accordance with these assumptions, analytical methods can then be used to derive predictions for the evolution of the X-ray luminosity function and its correlation with the cluster X-ray temperature (Kaiser 1986; Kitayama & Suto 1996; Mathiesen & Evrard 1998; Viana & Liddle 1999).

Given the wealth of information which can be obtained from observations of X-ray clusters, a lot of efforts have been devoted to obtaining directly the gas and temperature distributions, using numerical simulations for investigating the evolution of galaxy clusters. Collisionless N-body simulations have been used to study substructure formation (West, Oemler & Dekel 1998; Crone, Evrard & Richstone 1996; Buote & Xu 1997; Jing et al. 1995), density profiles (Crone, Evrard & Richstone 1994; Huss, Jain & Steinmetz 1999; Moore et al. 1998; Jing & Suto 2000), and statistical properties in a cosmological volume (Eke, Cole & Frenk 1996; Lacey & Cole 1994). In these simulations the dark matter distribution is a good tracer of that of the gas provided that the cluster dynamical state is not far from equilibrium, with a small fraction of substructures within the virial radius. Furthermore, the dark matter density profile shows no evidence for a core radius (Moore et al. 1998) whatever numerical resolution is achieved. Numerical simulations have then been extended to include the hydrodynamics of the gaseous component. The numerical methods used are either Eulerian (Cen & Ostriker 1994; Anninos & Norman 1996; Brian & Norman 1998; Kang et al. 1994; Bryan et al. 1994; Cen 1997; Cen et al. 1995), with a fixed or adaptative grid, or Lagrangian (Evrard 1988, 1990; Thomas & Couchman 1992; Navarro, Frenk & White 1995; Eke, Navarro & Frenk 1998; Katz & White 1993; Yoshikawa, Itoh & Suto 1998; Valdarnini, Ghizzardi & Bonometto 1999). The Lagrangian schemes are based on the smoothed particle hydrodynamic technique (SPH: Gingold & Monaghan 1977; Monaghan 1992). In these simulations the required dynamical range can be quite demanding. A large simulation box is needed in order to obtain a meaningful statistical sample of galaxy clusters; at the same time the minimum spatial resolution must be at

least close to the cluster core radii, where the bulk of the X-ray emission originates. For Lagrangian methods a partial solution is the multimass technique (Katz & White 1993), where the particles increase their masses according to their distance from the cluster center. A single cluster can then be simulated with a comparatively high numerical resolution, with external shells of matter surrounding the cluster and representing the large-scale gravitational field. In these simulations the gas component is treated as a single adiabatic fluid, without taking into account the effects of radiative cooling, and the physical processes of merging, substructure formation, shocks and compressional heating of the gas can be modelled in this way. A comparison between different numerical simulations shows that they are successful in reproducing the gross features of the cluster properties (Frenk et al. 1999).

The inclusion of radiative cooling for the gas is important on scales where the gas cooling time is shorter than the Hubble time. For galaxy clusters the spatial extent of this region is between 50 and 200 Kpc from the cluster center. A gas cooling radius r_{cool} can then be defined where the two time scales are equal. There is observational evidence that numerical simulations must include radiative cooling, together with star formation and energy feedback, in order to model adequately the relevant physical processes of the gas during its evolution. In the inner regions where the radiative time scales are short, a cooling flow develops (Fabian 1994), with $r_{cool} \simeq 50h^{-1}Kpc$. More than 50% of clusters are estimated to have their cores in this phase (Peres et al. 1998). These instabilities can affect several properties, like the $L_X - T_X$ relation (Fabian et al. 1994; Allen & Fabian 1998a; Markevitch 1998). In addition to cooling flows there is also strong observational support for non-gravitational heating of the cluster gas. Simple scaling arguments predict $L_X \propto T_X^2$ (Kaiser 1986), while the observed relation satisfies $L_X \propto T_X^3$ (David et al. 1993). This discrepancy has been suggested by many authors (Evrard & Henry 1991; Wu, Fabian & Nulsen 1998; Ponman, Cannon & Navarro 1999) as being evidence for substantial heating of the intracluster gas due to energy injection by supernova explosions at high redshifts. Another central question for including star formation in simulations of the gaseous component is the growing observational evidence for radial gradients in the iron abundance (Ezawa et al. 1997; Fukazawa et al. 1998), with possible connections to cooling flows (Allen & Fabian 1998b).

With increasing availability of computational power, numerical hydrodynamical simulations have attempted to model the effects of radiative cooling of the gas in the formation and evolution of cluster galaxies (Katz & White 1993; Sugimotohara & Ostriker 1998; Anninos & Norman 1996; Yoshikawa, Jing & Suto 2000; Pearce et al. 2000; Lewis et al. 2000). The numerical problems posed by the inclusion of gas cooling are challenging, mainly because the required increase in spatial resolution also requires that one keeps two-body heating mechanisms under control. Moreover, it will be seen that the inclusion of radiative cooling for the gas cannot be separated from considering also star formation and energy feedback from

SN explosions, in order to obtain realistic cluster density profiles and luminosities. Previous simulations have produced some conflicting results (Yoshikawa, Jing & Suto 2000; Pearce et al. 2000), and so the question of the minimum resolution in this kind of simulation is still to be fully settled. The purpose of this paper is to test the numerical reliability of SPH hydrodynamical simulations of cluster formation. These simulations will include the effects of radiative losses, star formation and energy feedback from SN. Four different clusters from two cosmological models have been studied in several simulations with different numerical inputs and star formation modelling. Final profiles are compared in order to assess the effects on the integrations of numerical resolution, and different star formation prescriptions. The paper is organized as follows. In §2 I describe the hydrodynamical simulations with radiative cooling and star formation that have been performed. The simulation results are then discussed in §3. In particular, §3.1 is dedicated to a comparison between different runs of the final radial density and temperature profiles, as well as of the X-ray luminosities. In §3.2 the simulation results are compared with previous findings. In §3.3 simulation runs with different star formation prescriptions are performed for a chosen test cluster which showed a well defined cooling instability. In §3.4 simulation results for runs with different prescriptions for star formation are compared against observed data from cooling flow clusters, in order to assess the consistency with real data for the assumed star formation models in the simulations. Finally the main conclusions are summarized in §4.

2. Simulations

In a previous paper (Valdarnini, Ghizzardi & Bonometto 1999, hereafter VGB) a large set of hydrodynamical simulations was used to study global X-ray cluster morphology and its evolution. The simulations were run using a TREESPH code with no gas cooling or heating. In order to assess the numerical reliability of the numerical integrations, four different clusters were selected as a representative sample of all of the simulation clusters. For this cluster sample, a large set of different integrations was performed by varying two numerical input parameters: the number of particles and the softening parameter. A comparison between the final gas density and temperature profiles, as well as with X-ray luminosities, then allowed the two-body heating to be kept under control and a fairly safe range of allowed values for the numerical parameters to be established. The simulation tests showed the relative importance of different numerical effects in these adiabatic simulations. It is therefore natural to use the same cluster sample to study the effects of including additional physics such as gas cooling and star formation. A comparison with the previous tests in VGB will show, with respect to the adiabatic case, the effects on the final cluster properties of considering energy sinks and non-gravitational heating. Here I give a short description of the cluster simulations

performed in VGB; the reader is referred to the original paper for more details. Numerical modelling of gas cooling and gas conversion into collisionless stars is described later.

In VGB three spatially flat cosmological models have been considered. A standard cold dark matter model (CDM), a vacuum-energy dominated model with $\Omega_\Lambda = 0.7$ (Λ CDM) and a mixed dark matter model (CHDM). For the Hubble constant $H_0 = 100h \text{ Km sec}^{-1} \text{ Mpc}^{-1}$, $h = 0.5$ is used for CDM and CHDM and $h = 0.7$ for Λ CDM. For all models, the primeval spectral index $n = 1$ and the baryon density parameter $\Omega_b h^2 = 0.015$. For CHDM $\Omega_h = 0.20$ is the HDM density parameter of massive neutrinos; only one massive species is considered. All of the models were normalized in order to reproduce the present cluster abundance (Eke, Cole & Frenk 1996; Girardi et al. 1998). The cosmologies were chosen in order to have simple models with different properties. For each model an N-body cosmological simulation was first run in a $L = 200h^{-1} \text{ Mpc}$ comoving box using a P^3M code. The particle number were $N_p = 10^6$ for the CDM and CHDM models with $\Omega_m = 1$, while $N_p = 84^3$ for Λ CDM with $\Omega_m = 0.3$. The same random numbers were used to set the initial conditions for all three cosmological models. The simulations started from an initial redshift z_{in} . At $z = 0$ clusters of galaxies were located using a friends-of-friends (FoF) algorithm, so as to detect overdensities in excess of $\simeq 200\Omega_m^{-0.6}$. For statistical analysis, VGB selected for each model the 40 most massive clusters. For each of these clusters a TREESPH hydrodynamical simulation was performed in physical coordinates. The integration was accomplished by first locating at $z = 0$ the cluster center and identifying all of the simulation particles of the cosmological simulation within r_{200} , where the cluster density is $\simeq 200\Omega_m^{-0.6}$ times the background density. These particles are located back at z_{in} , in the original simulation box, and a cube of size L_c enclosing all of them is then found, with a size $\simeq 15 - 25h^{-1} \text{ Mpc}$. A lattice of $N_L = 22^3$ grid points is set inside this cube; different lattices were used for each matter component. At each node position is associated a particle of corresponding mass and coordinates. The particles were then perturbed, using the same random realization as for the cosmological simulations. Additional frequencies are introduced so to sample the higher Nyquist frequency. The baryon particles are perturbed identically to the CDM particles and their initial temperature is set to $T_i = 10^4 \text{ }^\circ\text{K}$. For the TREESPH simulations all the particles which lie inside a sphere of radius $L_c/2$ are kept. External gravitational fields are modelled by considering a larger cube of side $2L_c$, inside the cube particle positions are set as for the smaller cube, but with no gas. The number of grid points is the same as for the inner cube, so that masses are 8 times larger than those of the inner cube; particles of the larger cube are considered only outside the smaller one. After the particle positions are perturbed, only those within a sphere of radius L_c from the cluster center are kept for the TREESPH simulations. This multimass grid technique has already been used in cluster simulations by Katz & White (1993) and Navarro, Frenk and White (1995).

For each particle, the gravitational softening parameters are set according to the scaling $\varepsilon_i \propto m_i^{1/3}$. The numerical integrations were performed with a tolerance parameter $\theta = 0.7$, without quadrupole corrections. The reliability of the numerical resolution was tested in VGB by taking the most massive and least massive clusters (labels 00 and 39, respectively) for the two models CHDM and Λ CDM. For each of them, different numerical tests were carried out. Accordingly to VGB, the cluster simulations can be performed with an adequate resolution using a number of gas particles $N_g \gtrsim 5,000$ and a gas softening parameter $\varepsilon_g \lesssim 50h^{-1}Kpc$. For the collisionless component the corresponding values are scaled accordingly. In Table 1 the reference values for the four clusters are given. If one introduces radiative cooling then the final values for the core radius of the gas density are expected to be smaller than in the no-cooling case. This implies that the numerical simulations must have smaller values for the gas softening ε_g , which in SPH sets a minimum resolvable scale, since SPH smoothing lengths are constrained to be $\gtrsim \varepsilon_g/4$. The shape of the density profile implies, with respect to the adiabatic case, higher values for the gas and dark matter densities at the core radius. This in turn implies that larger values for the number of particles are required in simulations of cooling clusters. This is essential in order to reduce the values of particle masses and hence the two-body heating time τ_r , which approximately scales as $\tau_r \propto 1/(\rho_d m_d)$, where ρ_d and m_d are the dark matter density and particle mass.

In order to check for these numerical effects, for each of the four test clusters a set of five TREESPH simulations was performed, using the same initial conditions and with the inclusion of radiative cooling, but for different values of ε_g and N_g . With respect to the reference case, the other matter components have their particle numbers changed in proportion to the change in N_g . For the cluster Λ CDM00, Table 2 reports the values of ε_g and N_g for the five simulation runs. Table 4 is for CHDM00. For these two clusters the generic simulation has cluster index cl00 – j , with $j = 00, 01, \dots, 05$. The cluster cl00 – 00 is the reference case without cooling. The simulations have been carried out with the same values for the other numerical parameters that were used in VGB, with the difference that here the minimum allowed time step for gas particles is $\Delta t_m = 6.9 \cdot 10^5 yr$. For the clusters Λ CDM39 and CHDM39, the parameters of the numerical tests cl39 – j are given in Table 5. For these simulation runs, the number of particles and the initial redshifts are the same as for the 00 clusters. Therefore Table 5 reports only the particle masses and softenings. The effects of radiative cooling are modelled in these simulations by adding to the SPH thermal energy equation an energy-sink term (Hernquist & Katz 1989, eq. [2.29]). The total cooling function includes contributions from recombination and collisional excitation, bremsstrahlung and inverse Compton cooling. For cluster temperatures which satisfy $T \gtrsim 2KeV$, a condition which is always satisfied for the cluster sample studied here, the dominant cooling mechanisms are free-free transitions, but line cooling becomes important for small clusters

and groups. For the same reason, heating from an ionizing UV background is not included in the thermal energy equation. The radiative cooling is computed for a gas having primordial abundances $X = 0.75$, $Y = 0.25$ with zero metallicity. In the simulation runs where the gas particles are allowed to convert part of their mass into stars (see below), the back effects of metallicities on the cooling function are neglected. This is a valid approximation as long as $T \gtrsim 2\text{KeV}$ and stellar metallicities are below $Z \lesssim Z_{\odot}$ ($[Fe/H] \lesssim 0$) (Brian & Norman 1998; Carraro, Lia & Chiosi 1998).

In addition to these simulations, which include the effects of radiative cooling, a mirror simulation was performed for each of them. The mirror runs had an additional prescription which allowed eligible gas to be turned into stars. These simulations are indexed as cl00 – k and cl39 – k , where $k = j + 5$ and j is the index of the pure cooling runs in Tables 2, 4 & 5. For the cluster ΛCDM00 the simulation parameters for the cooling runs with star formation, cl00 – k , are given in Table 3. The numerical parameters of the simulations with radiative cooling and star formation are the same as the corresponding cooling simulations. For this reason Table 3 reports parameters only for the cluster ΛCDM00 . The additional simulation with $k = 11$ in Table 3 has the same parameters as the $k = 10$ run, but with $\theta = 1$ and quadrupole corrections, instead of $\theta = 0.7$. This is done in order to check the accuracy of the gravitational integration when a collisionless population, with a different distribution from that of dark matter, is added to the simulation. Allowing the gas to cool radiatively will produce dense clumps of gas at low temperatures ($\simeq 10^4 \text{ }^\circ\text{K}$). Thus cooling times will become shorter and even denser regions will develop. This is known as the overcooling instability (Suginohara & Ostriker 1998). In these regions the gas will be thermally unstable and will meet the physical conditions to form stars. In TREESPH simulations, star formation (SF) processes have been implemented using two different algorithms (Katz 1992; Navarro & White 1993). According to Katz (1992), a gas particle is in a star forming region if the flow is convergent and the local sound crossing time is larger than the dynamical time (i.e. the fluid is Jeans unstable). These two conditions read

$$\begin{cases} \nabla \cdot \vec{v}_i < 0 \\ h_i/c_i > \sqrt{3\pi/16G\rho_i} \equiv \tau_d, \end{cases} \quad (1)$$

where \vec{v}_i is the particle velocity, h_i the SPH smoothing length and c_i is the local sound velocity. In a more refined version, Katz, Weinberg & Hernquist (1996, hereafter KWH) introduced two additional requirements: a star forming region must have a minimum physical hydrogen number density $n_H = 0.1\text{cm}^{-3}$ and the local gas density must satisfy $\rho_g/\bar{\rho}_g > 55.7$ (this follows from an isothermal profile giving a mean virialized overdensity of $\simeq 169$). If a gas particle meets these criteria then it is selected as an eligible particle to form stars. In regions where the gas density is depressed because of gravitational softening, the Jeans

criterion is not applied, in order to avoid an underestimate of the local star formation rate (SFR) (Katz 1992, eq.[2]). The local SFR obeys the equation

$$d\rho_g/dt = -c_\star\rho_g/\tau_g = -d\rho_\star/dt , \quad (2)$$

where ρ_g is the gas density, ρ_\star is the star density , c_\star is a characteristic dimensionless efficiency parameter, τ_g is the local collapse time (the maximum of the local cooling time τ_c and the dynamical time τ_d). Gas particles with $T \lesssim 10^4 \text{ }^\circ\text{K}$ have long cooling times and $\tau_g = \tau_d$. The probability that a gas particle will form stars in a time step Δt is given by

$$p = 1 - \exp(-c_\star\Delta t/\tau_g). \quad (3)$$

A uniform random number ξ_r is generated at every time step for each of the gas particles satisfying the star formation criterion, and equation (3) is used to compute the formation probability p . If $\xi_r < p$ then a mass fraction ε_\star of the mass of the gas is converted into a new collisionless particle. This star particle has the position, velocity and gravitational softening of the original gas particle. Typical assumed values are $\varepsilon_\star = 1/3$ and $c_\star = 0.1$ (KWH).

The second algorithm for implementing SF in TREESPH simulations has been introduced by Navarro & White (1993 , hereafter NW). According to NW, any gas particle which is in a convergent flow and for which the density exceeds a threshold , i.e.

$$\begin{cases} \nabla \cdot \vec{v}_i < 0 \\ \rho_g > \rho_{g,c} = 7 \cdot 10^{-26} \text{ gr cm}^{-3}, \end{cases} \quad (4)$$

will have cooling time shorter than the dynamical time and will soon cool to $T \lesssim 10^4 \text{ }^\circ\text{K}$, thus satisfying the Jeans instability criterion. The two conditions (4) are necessary and sufficient conditions for selecting gas particles as prone to SF. For the local SFR, NW adopted equation (2) with $c_\star = 1$, $\tau_g = \tau_d$ and $\varepsilon_\star = 1/2$ as the condition for which a gas particle can convert part of its mass into a star particle. These two algorithms will be referred to hereafter as KWH and NW, respectively.

The numerical tests cl00 – k and cl39 – k have been performed following the NW prescription for selecting gas particles which can form stars. The NW method has been preferred over KWH because of its simpler assumptions about the physical conditions of the gas in star forming regions. Because of the many physical processes involved in SF, having a minimal number of assumptions can reduce possible biases in hydrodynamical simulations when modelling the local SFR. For a single representative cluster, a detailed comparison has been made between the cluster properties obtained using the two methods and different input values for the SF parameters. These simulation runs with numerical modelling of SF

also include energy feedback to cluster gas from supernova (SN) explosions. Once a star particle is created it can release energy into the surrounding gas through SN explosions. This energy is converted into heat of the neighboring gas at each time step, according to the stellar lifetime and initial mass function. A standard Miller-Scalo (1979) mass function has been adopted in the mass range from 0.1 to $100M_{\odot}$. All of the stars with masses above $8M_{\odot}$ end as SNe, leaving a $1.4M_{\odot}$ remnant. Each SN explosion produces $\varepsilon_{SN} \simeq 10^{51}$ erg, or $\simeq 7.5 \cdot 10^{48}$ erg / M_{\odot} , which is added to the thermal energy of the gas. Current time steps are much smaller than stellar lifetimes, and so the SN energy is released gradually into the gas according to the lifetime of stars of different masses. At each time step, the fraction of stars releasing their energy into the medium is calculated for any star particle and the corresponding SN energy is spread over neighboring gas particles according to the SPH smoothing prescription. SN explosions also inject enriched material into the intracluster medium, thus increasing its metallicity with time. According to Steinmetz & Muller (1994) $p_Z = 0.357m - 2.2$ solar masses of heavy elements are synthesized by a SN progenitor of mass m . The enrichment in metals of the intracluster medium is modelled as follows (Steinmetz & Mueller 1994; Carraro, Lia & Chiosi 1998). Each SPH gas particle initially has zero metallicity; star particles are produced with the metallicity of the parent gas particle at the epoch of their creation. The metallicity of gas particles is successively enriched at each time step according to the fraction of exploding SNe associated with each star particle. The mass in metals produced by these explosions is calculated in accordance with the specified function p_Z , and is added to the metallicities of the gas neighbors of the star particle. This mass is distributed over the neighbors using a smoothing procedure identical to that implemented for spreading the SN feedback energy of star particles among internal energies of the gas neighbors. According to the same procedure, the current mass fraction of exploding SNe with $M \geq 8M_{\odot}$ is also added to the mass of the gas particles, with the exception of the $1.4M_{\odot}$ remnant.

3. Results

3.1. Cluster simulations with radiative cooling and cooling plus star formation

The radial density and temperature profiles for the pure cooling runs are shown in Figures 1 & 2. The cluster center has been identified as the maximum of the gas density. For each radial bin spherical averaged quantities have been obtained by estimating hydrodynamical variables at 100 grid points uniformly spaced in angular coordinates. Densities and temperatures at the grid points were computed from SPH variables according to the SPH smoothing procedure. The cluster Λ CDM00 is a particularly neat example of the effects at

work in the simulations. As can be inferred from the softening values reported in Table 2, the numerical strategy has been first to run cl00 – 00 with the additional cooling prescriptions (cl00 – 01) and in subsequent runs the value of ε_g has been reduced in order to resolve the core radius of the gas density profile. Figure 1a shows that this is not achieved: whatever is the value of ε_g , there is no evidence of a gas core radius, the gas density continues to rise steeply at the cluster center without any indication of converging to a constant value. This result is in strict agreement with those of others (Suginohara & Ostriker 1998; Anninos & Norman 1996; Pearce et al. 2000; Lewis et al. 2000) and it is known as the overcooling instability; at the cluster center cooling times are very short because the gas density is high, thus drawing in more more material. The fact that the gas central density continues to rise as the spatial resolution is increased suggests that the extent of the (physical) effect is limited by the numerical resolution of the simulation. Of the four test clusters, CHDM00 is the only one which does not show the cooling instability with the exception of cl00 – 05 (Figure 2a). The reason for this behavior may be dynamical. Buote & Tsai (1996) measured a negative correlation of the cooling rate with the cluster X-ray substructure. The cooling instability can then be strongly suppressed when the cluster is still in a young dynamical state, with a large fraction of substructure. For the cosmology considered, VGB found that the clusters studied in the CHDM model with $\Omega_m = 1$ had many more substructures than those in the low-density Λ CDM model. In this case CHDM00 could be marginally stable, with instability being triggered by numerical effects when the central value of the gas density increases because the simulation resolution is increased.

In the simulation runs the number of particles was increased as ε_g was reduced so as to keep 2-body heating under control. The relaxation time τ_r , due to 2-body effects, is defined as

$$\tau_r = 0.34 \frac{\sigma_1^3}{G^2 m_d \rho_d \ln \Lambda} \simeq 6.7 \cdot 10^5 Gyr \left(\frac{\sigma_1}{10^3 K msec^{-1}} \right)^3 \times \frac{h^{-2}}{(m_d/10^{11} M_\odot)} \frac{1}{(\rho_d/\rho_c) \ln \Lambda} , \quad (5)$$

where σ_1 is the 1-D dark matter velocity dispersion, G is the gravitational constant, ρ_d is the dark matter density; $\ln \Lambda$ is the Coulomb logarithm, with $\Lambda \simeq R_h/4\varepsilon_g$, and R_h is the half-mass radius. Typical values are $\ln \Lambda \simeq 3$; standard theory gives $\Lambda \simeq R_h/\varepsilon$, the factor 4 above accounts for the softening bimodal distribution (Farouki & Salpeter 1982). For the simulations cl00 – 00 and cl39 – 00 the relaxation time τ_r has been estimated at radius $\simeq 0.05r_{200} \simeq 100Kpc$, approximately the resolution limit of these simulations. At this length scale $\rho_d/\rho_c \simeq 2 \cdot 10^4$. The values of τ_r range from $\simeq 13Gyr$ (cl00 – 00) to $\simeq 17Gyr$ (cl39 – 00). For the simulation runs with increased resolution the minimum resolvable scale is set by ε_g , and $\rho/\rho_c \simeq 5 \cdot 10^4$ at a fiducial scale $\simeq 50Kpc$. These rather high values of ρ_d are a consequence of the slightly steeper profiles for dark matter in the inner regions, with

respect to the case with no cooling. For these runs, the increase in ρ_d is compensated by a corresponding increase in the particle number and hence a smaller value for m_d , so that τ_r is approximately constant at the scale considered and is close to the Hubble time. Another timescale which is relevant for these simulations is the cooling time τ_c , defined as

$$\tau_c = \frac{3nk_B T}{2\Lambda_c}, \quad (6)$$

where k_B is the Boltzmann constant, n is the gas number density, T is the gas temperature and $\Lambda_c \simeq 5.2 \cdot 10^{-28} T^{1/2} n^2 \text{ergsec}^{-1} \text{cm}^{-3}$ is the cooling function. In the central gas regions $\tau_c \ll H_0^{-1}$ and a cooling instability will develop. In Figure 5 τ_c is shown as a function of radius for the four test clusters. For the cooling runs cl00 – 05, cl39 – 05 τ_c is always below $\simeq 20 \text{Gyr}$ for $r \lesssim 100 \text{Kpc}$, with the exception of $\Lambda\text{CDM}39$, which has a bump but then a strong fall in τ_c proceeding inwards. For the sake of reference, τ_c for the no-cooling case (–00) has also been plotted. Because of the presence of a gas core radius in this case τ_c approaches a constant value towards the center. According to Steinmetz & White (1997) gas cooling will be affected by artificial 2-body heating unless $\tau_c(r) < \tau_r(r)$. This condition is satisfied if the dark particle mass is smaller than the critical value

$$M_c = 2 \cdot 10^9 T_6 f_{0.05} M_\odot, \quad (7)$$

where T_6 is the the gas temperature in units of 10^6K , $f_{0.05}$ is the ratio $f = \rho_g/\rho_d$ in units of 0.05. For the simulated clusters studied here $T_6 \simeq 50 - 100$, $f_{0.05} \gtrsim 0.5$ for $r \lesssim 100 \text{Kpc}$ and M_c is always above m_d . The simulations can then be considered free from numerical effects which can dominate the gas behavior. In the cooling simulations this condition might be violated near the cluster center, where $T_6 \lesssim 10$ for $r \lesssim 50 \text{Kpc}$. However, in these regions $\tau_c \ll \tau_d \simeq 27 h^{-1} \text{Gyr} / \sqrt{\rho_d/\rho_c}$ and the cooling is effective in removing the gas energy at a faster rate than the one set by dynamical effects.

The temperature profiles show a decrease for $r \lesssim 100 \text{Kpc}$ and a drastic drop in the central values, where cooling is most effective. This inversion in temperature takes place in all of the tests considered. Peak values for the gas temperature are located at $\simeq 100 \text{Kpc}$ (0.05–0.1 of r_{200}). Between this distance from the cluster center and r_{200} the gas temperature decreases with radius and the clusters clearly cannot be considered isothermal. These results are in agreement with those of Pearce et al. (2000), and suggest that the global cluster properties are affected by cooling processes active on inner scales, where the cooling time is short (see also Lewis et al. 2000). The most important cluster variable which is affected by these results is the cluster X-ray luminosity. For evaluating L_X the standard SPH estimator

gives

$$L_X = 5.2 \cdot 10^{-28} \frac{1}{(\mu m_p)^2} \sum_i^{N_g} m_i \rho_i T_i^{1/2} \text{ergsec}^{-1}, \quad (8)$$

where, for the cooling function, the bremsstrahlung emissivity has been approximated with a gaunt factor of 1.2 (eq.[2] of Sugihara & Ostriker 1998), $\mu = 0.6$ is the mean molecular weight, and m_p is the proton mass. The summation is over all of the gas particles within r_{200} . Figure 7 shows the behavior of L_X at $z = 0$ as a function of ε_g for the pure cooling runs (open symbols). There is not a clear convergence of L_X as the resolution is increased. In fact L_X obeys the approximate scaling $L_X \propto 1/\varepsilon_g^5$. Similar results for L_X have been obtained by Anninos & Norman (1996) in their convergence study of simulations of X-ray clusters.

The unphysically high values found for L_X in the pure cooling runs arise because the gas density continues to increase steadily at the cluster center, while the conditions of high gas density and low temperature cause the gas to become Jeans unstable. Thus the treatment of gas cooling in cluster simulations cannot be decoupled from a modelling of the physical processes turning the cold, dense, gas into stars. The cooling simulations have therefore been rerun with the inclusion in the integrations of an algorithm for converting gas into stars. This used the NW method, with parameters $c_\star = 1$ and $\varepsilon_\star = 1/2$. In these simulations gas particles can produce star particles without any limit on the number of star-forming events. Furthermore, the SN explosion energies and metallicities that star particles can produce are smoothed over 32 gas neighbors but with an upper limit of $h_M = 15Kpc$ for the SPH smoothing length. This is in order to avoid unphysical heating of the gas over length scales much larger than those involved in the SF activities. This upper limit is also justified by the lack of diffusion in the ICM of the metals injected from galaxies (Ezawa et al. 1997). The results obtained are shown in Figures 3 and 4; the index of the simulations is $k = j + 5$, where j is the index of the cooling runs. The most important result is that the inclusion of an SF model has been effective in removing the unphysical gas behavior, which now shows a well defined core radius in the radial density plots. This is valid in all of the cases considered, with the exception of CHDM00. The simulation runs cl00 – k do not show, for this cluster, evidence of an SF activity, a result which is in agreement with the lack of a cooling instability in the cooling simulations cl00 – j . The shapes of the temperature profiles show that convergence is achieved for $N_g \gtrsim 20,000$. For the simulation runs with the highest resolution, all of the central values for the gas temperatures at $r = 10Kpc$ are within a factor $\simeq 1.5$. CHDM39 is an exception to this rule, with cl39 – 10 still not showing a flat temperature profile in the inner regions and resembling that of cl39 – 05. It is unlikely that the source of the discrepancy is due to a convergence problem: cl39 – 11 has a slightly larger accuracy in the computation of the gravitational forces (Hernquist 1987),

nevertheless its temperature profile has these discrepancies largely removed. For CHDM39 the peculiarity of cl39–10 in the final temperature profile, with respect to the other numerical tests shown in Figure 4b, could be of a numerical nature: for a certain accuracy in the tree evaluation of the gravitational forces, matter subclumps might form during the integrations which can then modify the gas dynamics. The formation of these sub-clumps is triggered by the approximations involved in the truncation of the multipole expansion of the cluster gravitational potential. The statistical occurrence of this effect should be small, because it is not observed in the other three test clusters. For a tree method the errors involved in the multipole expansion of the gravitational potential have been estimated by Hernquist (1987) assuming a spherical, isotropic Plummer model for the mass distribution of N test particles. A comparison against the accelerations obtained by a direct sum shows that in the large N limit ($N \gtrsim 30,000$) the errors in the tree evaluation of the accelerations are negligible for a monopole expansion if $\theta \lesssim 1$. The inclusion of the quadrupole terms improves the accuracy of the force computation, for $\theta \simeq 1$ the errors in the forces are those of a monopole expansion with $\theta \simeq 0.8$. The convergence in $T(r)$ obtained for cl39 – 11 suggests that for a given accuracy, quadrupole corrections should be preferred when evaluating tree forces.

The radial density profiles of the star component are also shown for the various runs in the density plots. The slope of these profiles is approximately $\simeq -3$, a value close to the one observed for galaxy populations in galaxy clusters. In all of the simulations, the gas density profiles have a well-defined core radius, with size $r_c \simeq 50 - 100 Kpc$, approximately 0.05 of the virial radii. From the density profiles note also that the gas core radii are smaller than in the no-cooling runs, outwards of r_c the density profiles are very similar to the no-cooling cases. The temperature profiles increase inwards from the virial radius up to $\simeq 100 - 200 Kpc$. Thereafter the profiles stay almost flat, or with a modest decrease in $T(r)$ towards $r = 0$. The strong drop of the temperatures in the very central regions for the cooling runs is no longer seen, the inclusion of a star formation prescription having been effective in removing the cold gas particles ($\lesssim 10^4 K$) from the cluster centers.

Cooling timescales $\tau_c(r)$ are plotted in Figure 5; the dashed line in the four panels is for the simulation runs including SF. As a general rule, for each test cluster, the τ_c are almost indistinguishable in all of the simulation tests for $r \gtrsim 100 Kpc$. In the simulations including SF, τ_c moves toward the no-cooling case in the cluster inner regions because of the reduction in the gas central density. The central values of τ_c are well below the present age of the universe for all of the models, with the exception of CHDM00. This cluster does not show a cooling instability and has $\tau_c \simeq 20 Gyr$ in the cluster core. Accretion rates $\dot{M}(r) = 4\pi\rho_g r^2 v_r$ are plotted in Figure 6 for the same test clusters as in Figure 5. For each radial bin, spherical averages of $\dot{M}(r)$ are shown only for negative values of v_r . For the test clusters in the Λ -dominated cosmology there is a well defined radial infall of matter within

$r \lesssim 100Kpc$, compared to the adiabatic run. These inflows of matter can be compared with those estimated from X-ray data for cooling flow clusters. For example Thomas, Fabian & Nulsen (1987) present mass deposition profiles $\dot{M}(< r)$ for a sample of 11 cooling flow clusters. They obtain for Abell 478 $\dot{M} \simeq 10^3 M_\odot yr^{-1}$ at $r \simeq 300Kpc$ (Fig. 7 of their paper). For this cluster they quote a measured line-of-sight velocity dispersion of $\simeq 750K msec^{-1}$ and the estimated cluster virial mass ($\simeq 4 \cdot 10^{14} h^{-1} M_\odot$) is close to that of Λ CDM39. This accretion rate is in good agreement with the values shown in Figure 6 at $r \simeq 300Kpc$ for Λ CDM39 in the simulation including SF. Note that in order to compare $\dot{M}(< r)$ with $\dot{M}(r)$ one is implicitly assuming a steady-state. The clusters in the cosmology with $\Omega_m = 1$ show values of \dot{M} which are higher in the adiabatic case, in comparison with the simulation runs including cooling and star formation. The reason for this discrepancy is of a dynamical nature: CHDM00, for example, has a large radial infall velocity because it is still out of equilibrium, with material collapsing onto the center. These results seem to support the hypothesis of an anti-correlation between the strength of the cooling flow and the dynamical state of the cluster, as measured by the power ratios, for example. Buote & Tsai (1996) demonstrated the existence of such an anti-correlation, as expected from a dependence of the cooling flow rate on the cluster dynamical state. A statistical analysis of this correlation is beyond the scope of this paper and is left to future work, where the analysis will be performed for the whole sample of 40 clusters for each of the three cosmological models (VGB). A striking result is the convergence of the final X-ray luminosities for the simulation runs including SF for the four test clusters. In Figure 7 the filled symbols refer to these simulations. The divergence for $\varepsilon_g \rightarrow 0$ of the cooling runs is completely removed and the plotted values are quite stable. An exception is cl39 – 10 of CHDM39 (the black square in the bottom right panel) which has $L_X \simeq 5 \cdot 10^{44} ergsec^{-1}$. As previously discussed, the peculiarity of this cluster is of a dynamical nature and there is not a question of convergence of hydrodynamical variables. In fact cl39 – 11 has $L_X \simeq 2 \cdot 10^{44} ergsec^{-1}$, a value in full agreement with the values of the other runs. Compared with the non-radiative case, the luminosities are stable (CHDM) or increase by a factor $\simeq 2$ (Λ CDM).

3.2. Comparison with previous simulations

These results can be compared with previous findings from hydrodynamical cluster simulations, in which the gas is allowed to undergo cooling and star formation or is subject to a prescription for the treatment of cold particles. The density plots can be compared to analogous plots shown in Lewis et al. (2000). In their paper Lewis et al. analyzed five simulations of a cluster with $M_{200} \simeq 4 \cdot 10^{14} M_\odot$ in a CDM universe with $\Omega_m = 1$ and $h = 0.5$. Of these simulations, the *Cool + SF* allows gas to undergo cooling and star formation, using

the KWH method with $c_* = 0.1$ and $\varepsilon_{SN} = 1$. Although the cosmologies are different, a rough comparison can be made for Λ CDM39, which has the closest virial mass to their test cluster. For Λ CDM39 the simulations cl39 – 10 or cl39 – 11 have a numerical resolution comparable to the Lewis et al. (2000) simulations (compare Tables 3 & 4 with Table 2 of Lewis et al.). Thus the density plots in Figure 3b can be compared with Figure 7 of Lewis et al. . The results are encouraging, there is a rough agreement for the various baryonic components, although in Lewis et al. there is a central spike in the gas density which is not observed in the present simulations. A substantial difference is instead found for the temperature profiles: all of the simulation runs show a tendency for $T(r)$ to recover an almost flat behavior in the inner regions (with the exception of cl39 – 10 for CHDM39, which is peculiar for the reasons previously outlined). Lewis et al. found instead that $T(r)$ in their *Cool + SF* simulation reaches a peak value of $\simeq 8 \cdot 10^7 \text{ }^\circ K$ within $\simeq 40 Kpc$ (Figure 9 of Lewis et al.). The radial behaviors of Figure 5 ($\tau_c(r)$) compare well with Figure 8 of Lewis et al. (2000).

Hydrodynamical simulations of cooling clusters have also been analyzed by Pearce et al. (2000) and Yoshikawa, Jing & Suto (2000). I discuss here in detail how the results of §3.1 compare with the cluster properties of Yoshikawa, Jing & Suto (2000, hereafter YJS). The simulated clusters of the Pearce et al. (2000) runs have properties similar to the YJS clusters, the only substantial differences being found for the X-ray luminosities.

In their paper YJS analyze results from a set of cosmological SPH simulations and concluded that estimates of the X-ray luminosities are biased by the numerical resolution of the simulations and are not reliable. The cosmological simulations of YJS were performed in a flat, Λ -dominated CDM cosmology. The values of the background cosmological parameter are identical to the ones chosen here for the cluster simulations in the Λ CDM model. They performed simulations with two different box sizes : $L = 75h^{-1}Mpc$ and $L = 150h^{-1}Mpc$. They took 128^3 gas particles, an equal number of dark particles, and a comoving softening parameter $\varepsilon = L/1280$. In the simulations including radiative cooling, cold gas particles were removed from the summations defining local gas variables if the Jeans condition in equation (1) is satisfied (simulation runs with label UJ in their notation). This constraint is slightly different from the one of Pearce et al. (2000), but is almost identical for $T_i \lesssim 10^4 \text{ }^\circ K$. Their prescription is phenomenological and is intended to take into account the process of galaxy formation. For the cosmological simulation with box size $L = 150h^{-1}Mpc$, the numerical resolution for the most luminous clusters is comparable to that of the cl00 – 11 run. The most massive cluster in the simulation with label 150UJ has $\simeq 1.56 \cdot 10^{15} M_\odot$, a value close to that of M_{200} in Table 1 for Λ CDM00. For this cluster YJS found at $z = 0$ a bolometric X-ray luminosity $\simeq 2 \cdot 10^{45} \text{ ergsec}^{-1}$, about twice the corresponding value of L_X for cl00 – 11. A comparison between the cluster density and temperature profiles (Figure 1 of their paper,

central panel) and the analogous plots of the present paper (cl00 – 11 in Figure 3) shows that there are substantial differences at $r \lesssim 50Kpc$. In YJS the cluster gas density shows no evidence for a core radius; the mass-weighted temperature profile has an inversion at the cluster center, as also found by Pearce et al. (2000), while cl00 – 11 shows a nearly flat profile for $T(r)$. These differences in the gas profiles at the cluster centers are probably due to the different methods employed for the treatment of the cooled gas, rather than to the numerical resolution of the simulations.

YJS adopted the phenomenological prescription of treating separately those gas particles which satisfy the Jeans criterion. Therefore the gas distribution consists of gas particles in a ‘hot’ X-ray emitting phase together with a population of cold particles at temperatures around $10^4 \text{ }^\circ K$, the latter being localized at the cluster center. The temperature profiles in YJS include the cold gas population ¹ and show a steep decrease at the cluster center. In the simulation run cl00 – 11 this is not observed because the star formation prescription has been effective in converting the cooled gas at the cluster center into the form of stars. For the simulation runs with cooling and star formation, the mass-weighted temperatures $T_m(sim)$ of the clusters Λ CDM00 and Λ CDM39 can be compared with those expected from the isothermal mass-temperature relation. At the present epoch, this relation reads:

$$k_B T_X \simeq 5.2\gamma \left(\frac{\Omega_m \Delta_c}{178} \right)^{1/3} \left(\frac{M}{10^{15} h^{-1} M_\odot} \right)^{2/3} \text{ KeV}, \quad (9)$$

where M is the cluster virial mass, $\Delta_c \simeq 178\Omega_m^{-0.55}$ is the virialized cluster overdensity and γ is a fudge factor. YJS found that the mass-weighted temperatures of their simulated clusters are well fitted by equation 9 with $\gamma = 1.2$. For the cluster Λ CDM00 (Λ CDM39) I find from the simulations cl00 – 11 (cl39 – 11) that $T_m(sim) = 5.6(3.1) \text{ KeV}$, while the theoretical relation (9) gives $T_m(th) = 5.9(2.8) \text{ KeV}$. Thus the mass-weighted temperatures of the simulated clusters are in close agreement with the theoretical predictions and also with those found by YJS in their simulations.

As previously shown in the simulation runs including star formation, the X-ray luminosities are found to be numerically stable and converging to reliable values. With respect to the adiabatic runs, the L_X are found to be constant or with a modest increase (Figure 7). These results are at variance with those of Pearce et al. (2000), who found that cooling clusters are less luminous than those in the no-cooling runs. Similar results have been obtained by YJS and Lewis et al. (2000), who measured an increase in the final X-ray luminosity when cooling was included. A comparison with the Cool+SF simulation of Lewis et al. (2000) is difficult

¹K. Yoshikawa: private communication

because of the different cosmologies and cluster virial masses. YJS analyzed the $L_X - T_X$ relation obtained from the simulated clusters in the UJ test runs at $z = 0$, from the simulations with two different box sizes. The cluster luminosities in the simulation with $L = 150h^{-1}Mpc$ are found to be underestimated with respect to the ones of the $L = 75h^{-1}Mpc$ simulation box. YJS draw the conclusion that, in order to have reliable cluster luminosities, simulations of cooling clusters require a much higher numerical resolution than the one employed in their simulations. In the simulations with $L = 150h^{-1}Mpc$, the mass of the gas particles is $\simeq 2 \cdot 10^{10}M_\odot$, a factor $\simeq 2$ larger than that of cl00 – 10 for Λ CDM00. Therefore their conclusion seems to be in conflict with what is claimed here, that substantial convergence in X-ray luminosities is achieved for the highest resolution simulation runs. The source of this discrepancy lies in the different numerical approaches. YJS simulated cluster evolution in a cosmological box with a constant gas particle mass. As outlined by the authors, the resolution problem is severe for the less luminous clusters in the simulation box. The multi-mass technique described in §2 is instead used here to simulate a single cluster. The results of the numerical simulations show that convergence in the gas variables is obtained for each *single* cluster whenever $N_g \gtrsim 20,000$. A comparison with the numerical resolution adopted by YJS is useful. In their simulations with $L = 150h^{-1}Mpc$ the gas particle mass is comparable to the value found here for which Λ CDM00 can be safely analyzed. However they have a constant mass resolution and their cluster sample has a lower limit of $M > 10^{14}M_\odot$. An application of the numerical parameters required here to a cluster with a virial mass of $\simeq 10^{14}M_\odot$ would give a gas particle mass of $\simeq \Omega_b 10^{14} / (\Omega_m 2.2 \cdot 10^4) \simeq 5 \cdot 10^8 M_\odot$, a factor $\simeq 30$ smaller than that being used in the $L = 150h^{-1}Mpc$ simulations. These values also show that cosmological simulations require a number of gas particles $\simeq (400L/150h^{-1}Mpc)^3$ in order to give realistic estimates for the statistical properties of X-ray clusters.

3.3. Simulations with different star formation prescriptions

The numerical tests studied here give the range of numerical parameters for which the results of cooling cluster simulations, including SF according to the NW prescription, reach numerical convergence and can be considered stable. A different question concerning the reliability of the numerical results is the sensitivity of the estimated cluster properties to the numerical method used to describe star formation and energy feedback from stars in the hydrodynamical simulations. To investigate this, final results for different simulations have been compared for a single test cluster (Λ CDM00). The simulations were performed with the same numerical parameters as for the cl00 – 11 run, but using different SF methods or parameters. This was done in order to demonstrate the effects of the SF modelling on the gas variables. A summary of these simulations with different SF prescriptions is reported in Table

6. The simulation with index I is the standard case with which previous cooling+SF runs have been performed. Thus this simulation just corresponds to cl00 – 11. Two simulation runs correspond to the NW method but with a different feedback energy for SN explosions (I and V). In the other three runs the KWH prescription was adopted for converting gas particles into stars. Two of them (II and III) compare the results obtained for a different star formation efficiency parameter c_* , with the other parameters being held fixed; in a third run (IV) the fraction ε_* of mass of the gas converted to stars is varied. The results of the different approaches are shown in Figures 8 & 9. For the simulation V, only the star formation rate (SFR) and the X-ray luminosity versus time have been plotted in the two left panels of Figure 8. This is because the simulation V produced final results almost identical to the reference case I. In simulation V the feedback SN energy was set to $\varepsilon_{SN} = 10^{50} \text{erg}$, a value ten times smaller than that of the simulation run I. A comparison between the results plotted in Figure 8 shows that the two simulations have an identical evolution for the X-ray luminosity, but a different SFR. This is because of the smaller amount of SN feedback energy which is added to the thermal energy of the gas in the run V. This in turn implies higher gas densities and SF rates for simulation V. The differences become negligible for $t \gtrsim 8 \text{Gyr}$. The final gas profiles, as well as the other variables, are identical.

The simulations with the KWH method and different ε_* (II and IV), give similar results and show that the choice of the mass fraction ε_* is not important in modelling the star formation processes. The most important differences are found between the KWH simulations with different c_* (II and IV). The differences are dramatic in the final X-ray luminosities, which differ by a factor $\simeq 40$. The source of this discrepancy lies in the different gas density profiles, which have substantial differences in the cluster core regions for $r \lesssim 100 \text{Kpc}$. These differences are localized at the cluster center; beyond $r \simeq 100 \text{Kpc}$ all of the profiles converge, as shown in the plots of Figure 8. The temperature profiles have a peak value of $\simeq 10^8 \text{K}$ at $r \simeq 100 \text{Kpc}$ and thereafter decline outwards by a factor ~ 2 out to r_{200} . Below $\sim 100 \text{Kpc}$ the profiles instead show large differences. Compared to run I (NW) the two simulations with $c_* = 0.1$ have gas temperatures which decrease inwards by a factor ~ 10 from $\sim 100 \text{Kpc}$ down to $r \sim 10 \text{Kpc}$. These radial decays follow because of the less efficient conversion of the cooled gas into stars compared to the NW run. These results can be compared with those of Lewis et al. (2000), who used the same star formation method and parameters, although in a different cosmology. The temperature profile of their Cool+SF simulation shows a similar decrease outside of the cluster core (Fig.9 of their paper). It is difficult to compare the radial runs at $r < 100 \text{Kpc}$ because the authors adopt a linear scale for the plots. The gas density profile of run II rises steeply towards the cluster center from $r \simeq 100 \text{Kpc}$; a similar behavior is shown by Lewis et al. (2000) for their hot gas population (see their Fig.7). The simulation run with $c_* = 1$ has radial profiles much closer (but not

identical) to the NW ones. These differences are also reflected in the estimated emission-weighted temperatures (see Table 6). For simulations I and III $T_{em} \simeq 8 - 9KeV$, while $T_{em} \simeq 2KeV$ for run II. Note that for this simulation most of the contribution to T_{em} comes from within the $50Kpc$ cluster core.

There is a remarkable agreement for the ratio of the cluster mass locked into stars to the gas mass, which is $\simeq 10\%$ at r_{200} for all of the runs considered (Figure 9, bottom left panel), with respect to the observational values (Evrard 1997). Also the density profiles of the stars produced are very similar. As a general rule, one can say that the global cluster properties are not affected by the SF prescription adopted. The source of the higher gas densities in the cluster core for the simulations with $c_\star = 0.1$, compared to what is found for $c_\star = 1$, is in the different SFR that the two simulations use during the integration. In the top left panel of Figure 8 the SF rates are plotted for the different runs. The rates are plotted versus time instead of redshift because otherwise final differences would have been compressed. It can be seen that the simulations II and IV have a different SF histories, with respect to runs III and I. At early times runs II and IV have a lower SFR than the simulation with $c_\star = 1$. This behavior is reversed after $t \simeq 10Gyr$ ($z \simeq 0.3$), with simulations II and IV showing a substantial SF activity, while runs III and I have a sharp decline in their SF rates. As final results, the two simulations II and IV have less gas converted to stars in the cluster core.

According to KWH, in a simulation with $c_\star = 0.1$, the collapsing gas will reach an equilibrium density higher than in the one with $c_\star = 1$. This is because of the reduced efficiency in the conversion of the gas into stars for the simulation with $c_\star = 0.1$, which implies that gas collapse will proceed until pressure from the thermal energy of the gas is able to prevent further gas collapse, reaching an equilibrium at higher gas densities. This in turn implies higher SF rates so that, after an initial transient, simulations with $c_\star = 0.1$ will have higher gas densities and SF rates compared to the $c_\star = 1$ runs. This expected behavior is what is found in the plots of Figure 8, the NW simulation giving identical results to the KWH run with $c_\star = 1$. The bottom right plot of Figure 9 shows $M_s(z)$ the cluster mass in stars at the redshift z and is particularly useful in analyzing differences in the SF histories between different runs. The mass in stars for the NW run stops growing at $z = 0.5$, and stays flat until $z = 0$. The KWH simulation with $c_\star = 1$ has a similar trend but with a somewhat steeper slope in the growth of $M_s(z)$. An important result is that the final values of the cluster mass in stars vary by only $\simeq 20\%$ from $M_s \simeq 1.5 \cdot 10^{13} M_\odot$. As previously outlined, this shows the reliability of different SF prescriptions in reproducing global cluster properties. In the simulation results, differences between the methods arise in the SF rates, which are determined by different choices of the star formation efficiency parameter c_\star . In Figure 9 for simulations II and IV, the values of $M_s(z)$ at high redshifts are below the corresponding values of the $c_\star = 1$ runs. For these simulations with $c_\star = 0.1$,

$M_s(z)$ has a continuous growth and is smaller than $M_s(z)$ of the NW run until $z \simeq 0.2$. Note that the final masses in stars for the different runs do not correspond to what would naively be expected from the different shapes of the gas density profiles in the cluster core, $M_s(z = 0)$ being determined by the overall SF history. The SF rates of the simulations with $c_\star = 0.1$ have the expected behavior, with respect to those of the $c_\star = 1$ runs, but the high resolution runs of the next section will show that these SF rates are depressed by the numerical resolution of the simulation.

The emission weighted metallicity profiles at $z = 0$ are shown in Figure 10. Conversion from the mass fraction in metals associated with each particle to the iron mass was accomplished according to the relationship between the total metallicity and the iron abundance $[Fe/H]$ of Tantalò, Chiosi & Bressan (1998). The relative iron abundances $Z = Fe/H$ in the radial bins were estimated from the individual iron mass of each gas particle using the SPH smoothing procedure. These profiles were still rather noisy, and to obtain the final radial profiles of iron abundance, a further smoothing was performed by considering only five distinct radial bins and averaging over neighboring bins. An important result for the metallicity profiles is that the simulation runs show the existence of radial gradients, with decreasing metallicities as the radius increases. This is in broad agreement with observational data for cooling flow clusters (Ezawa et al. 1997; Kikuci et al. 1999; Buote 2000; White 2000; De Grandi & Molendi 2001). For the simulation runs I and III $Z \gtrsim 0.5Z_\odot$ at the cluster center and $Z \lesssim 0.1Z_\odot$ at $r \gtrsim 100Kpc$, with a value for the solar abundance $Z_\odot = (Fe/H)_\odot \equiv 4.68 \cdot 10^{-5}$ (Anders & Grevesse 1989). At $r \gtrsim 100Kpc$ these values are $\sim 1/3$ of the measured abundances obtained for a sample of 9 cooling flow clusters (De Grandi & Molendi 2001). This deficit of iron abundance is probably due to the lack of metal enrichment of the intracluster medium from SN of type Ia and will be analyzed in a future paper, where the metallicity dependence of the cooling function will be implemented in the simulations. The KWH runs with $c_\star = 0.1$ have metallicity profiles with abundances well below the NW run, this is because of the different SF histories, with simulations II and IV having a lower SFR at early times ($\lesssim 10Gyr$). The KWH run with $c_\star = 1$ has, on average, a steeper metallicity gradient than the NW run; here again this is because of the different SF histories, as shown by the different growth of $M_s(z)$.

3.3.1. High resolution simulations with different star formation prescriptions

An important point about the simulation results related to the SF parameters, such as for example the SFR, is their dependence on the numerical resolution adopted. The numerical tests of Table 6 have been performed with the same number of particles and

softening parameters (cl00 – 11 in Table 3), and for the particle gas mass $m_g \simeq 1.2 \cdot 10^{10} M_\odot$. The resolution of the mass of gas is clearly inadequate for modelling a single galaxy formation process. SPH simulations of galaxy formation processes have been debated by many authors (Thacker & Couchman 2000, and references cited therein). In order to resolve the internal dynamics and to follow shock evolution of a forming galaxy a minimum of $\simeq 10^4$ particles is required (Thacker et al. 2000). Lia, Carraro & Salucci (2000) discussed the dependence of the mass resolution on the SFR in gas-dynamical simulations of a collapsing spheroid. According to their results, the total mass of gas converted into stars diminishes from 90% to $\simeq 80\%$ of the initial mass of gas, passing from the low resolution run with 2,000 particles to the high resolution run with more than $\simeq 10^4$ particles. However, early simulations (Evrard 1988, NW) showed that SPH simulations with even a small number of particles ($\simeq 100$) can converge to stable results as far as global properties are concerned. For example Figure 20 of NW indicates that the final mass of stars in their SPH simulations of a rotating cloud is already close to the convergence value for a number of gas particles $N_g \gtrsim 100$.

It is therefore important to assess the effects of numerical resolution on final results in the simulations with different SF prescriptions. This has been done by running again simulations I, II and III of Table 6 but with a number of particles increased by a factor $\simeq 3$. For the gas particles $N_g = 69,599$, $m_g = 2.4 \cdot 10^9 h^{-1} M_\odot$ and $\varepsilon_g = 10.5 h^{-1} Kpc$. The cold dark matter particles have these values scaled in proportion. These simulations will be referred as IH, IIH and IIIH, respectively. The numerical parameters are those of cl00 – 11H in Table 3. Different SF parameters correspond to the ones of Table 6. The simulation results are shown in Figure 11. For simulations IH there are not appreciable differences in the radial profiles. This confirms the results of §3.1, that the NW runs have reached numerical convergence in the physical variables for the numerical parameters of the cl00 – 10 simulation of Table 3. The profiles of simulation IIH are instead different from those of run II at $r \lesssim 50 Kpc$. The strong drop in $T(r)$ has been removed and the gas density profile is much closer to the NW one. Simulation IIIH gives final profiles very similar to the ones of the parent simulation. The bottom left panel of Figure 11 shows that high resolution runs have final X-ray luminosities which can differ by a factor ~ 2 from the parent simulations.

SF rates are shown in the the top left panel of Figure 11 and at $z > 0$ there are large differences between the high resolution run IIIH and the parent simulation. For $t \gtrsim 5Gyr$, simulations IH and IIIH give the best performances, with the SF rates closely following the ones of the lower resolution runs. Note the strong decline in the SFR after $z = 0.3$. At early times ($t \lesssim 5Gyr$) the SF rates of simulations I and III are much lower than those of the corresponding high resolution runs. For these runs, the peak of the SF activity is shifted from $z \simeq 0.7$ up to $z \simeq 2$ ($t \simeq 3Gyr$). This shows that in order to correctly sample the SF rate over the whole cluster evolution the numerical resolution must be at least that of

the high resolution runs. For $t \gtrsim 5Gyr$, simulations I and III have cluster SF rates in good agreement with those of the corresponding high resolution runs, while simulation II does not show that convergence is achieved when the resolution is increased. For simulations I and III, the X-ray variables are not affected by the undersampling of the SF rates at early times; for example, the X-ray luminosities (Figure 11, bottom left panel) are fairly stable under an increase in the numerical resolution.

The results of these high resolution simulations show that in the large N_g regime, different star formation methods approach similar gas profiles. For the simulations of Table 6, the differences found between the profiles of the runs with $c_\star = 0.1$ and the others arise because in the former case, with respect to the KWH run with $c_\star = 1$, the increase in the SF rate corresponding to a decrease in the value of c_\star is limited by the numerical resolution. The upper left panel of Figure 11 shows that for the high resolution run IIIH the SF rate is much higher than in simulation II.

From the simulation results it follows that the NW method is the most efficient in the removal of cold gas from the cluster center. As already stressed, in principle all the methods converge to the same profiles when N_{gas} gets very large. The runs with $c_\star = 0.1$ are the ones with the most important differences in the temperature profiles, compared to the other runs, and the reasons of these differences have been previously discussed. An explanation of why the NW method is so efficient relies on the chosen criterion for selecting cold gas subject to star formation, the method being based on a density threshold. If the local gas density ρ_i exceeds this threshold ($7.10^{-26} grcm^{-3}$) then a mass fraction $\varepsilon_\star = 1/2$ of the gas particle is converted into a star particle. In very high density regions, the timescales of star formation are very short and the SF process removes the gas very quickly. Because the criterion is based on a density threshold this means that *all* the gas particles above this threshold are selected for a star forming event.

Differences in the temperature profiles between the NW and KWH runs with $c_\star = 1$ are minimal and are localized at the cluster center, these differences being due to the different dependence of the two methods on the resolution limit of the simulations. The two criteria of SF depend on the numerical resolution of the simulations through the SPH smoothing lengths h_i , which determine ρ_i and are constrained by the lower limit $h_i \gtrsim \varepsilon_g/4 \equiv h_{min}$, where ε_g is the gravitational softening length. As the gas density increases toward the cluster center, the smoothing lengths h_i get smaller, until they reach the limit h_{min} . The results of the simulations show that at the cluster center, in the small value regime $h_i \rightarrow h_{min}$, the NW criterion for identifying cold gas particles is less sensitive to the resolution limit h_{min} than the KWH method based on the local Jeans instability.

To summarize, the above results demonstrate that simulations I and III of Table 6 have

an adequate numerical resolution to reliably predict X-ray cluster properties, such as the X-ray luminosity. For simulation II (KWH with $c_\star = 0.1$) there are still differences at the cluster core between the final profiles when the numerical resolution is increased. Run IIIH has a final L_X which is very large compared to the expected range of values from the luminosity-temperature relation (see below). For the simulation runs I and III $L_X \simeq 10^{45} \text{ergsec}^{-1}$, while $L_X \simeq 4 \cdot 10^{46} \text{ergsec}^{-1}$ for the runs with $c_\star = 0.1$. These large discrepancies can be reduced by adopting the phenomenological prescription of removing from the summation (8), cold gas particles with temperatures below a cut-off value T_c . For the runs II and IV with $c_\star = 0.1$, $L_X \simeq 10^{45} \text{ergsec}^{-1}$ if the above prescription is adopted with $T_c \simeq 3 \cdot 10^7 \text{K}$. It is important to note that the NW run has an L_X that shows no sign of evolution for $t \gtrsim 5 \text{Gyr}$ ($z \lesssim 1.2$).

3.4. Comparison with observational parameters

These differences between different methods suggest that a reliable SF algorithm should be chosen by requiring that simulation results should consistently satisfy a wide set of different observational constraints on cluster properties. To this end, the results of the simulation runs reported in Table 6 have been compared with several cluster observations. The data investigated are : the $L_X - T_X$ relation for cooling flow clusters and the estimated SFR in rich clusters at the present epoch. These observations have been chosen because the plots of Figure 8 showed large differences between simulated clusters for the variables connected with these data.

For cooling flow clusters, Allen & Fabian (1998a) have studied the relation between the bolometric X-ray luminosity L_{bX} and the cluster temperature. They use *ASCA* spectra and *ROSAT* images to construct a sample of 30 luminous clusters ($L_{bX} > 10^{45} \text{ergsec}^{-1}$), 21 of which have central cooling times $< 10 \text{Gyr}$ and are identified as cooling flow (CF) clusters. Their best-fit relationships are derived for a cosmology with $\Omega_m = 1$ and $h = 0.5$, thus the values reported in Table 1 of their paper must be rescaled to those for a flat cosmology with $\Omega_m = 0.3$ and $h = 0.7$. Allen & Fabian (1998) fit the $L_{bX} - T_X$ relation with a power-law of the form $kT_X = PL_{bX}^Q$, where kT_X is the spectral fit temperature of a single isothermal model in *KeV* and L_{bX} is in units of $10^{44} \text{ergsec}^{-1}$. The data values used are those of model C in Table 1, which according to the authors gives the best χ^2 values. Thus the coefficients P and Q obtained here for the Λ -cosmology are those corresponding in Allen & Fabian (1998) to the χ^2 only for the entry CFs in their Table 2. The least-square estimator gives $P = 1.97 \pm 0.33$ and $Q = 0.42 \pm 0.05$, error bars are the one-parameter 68% confidence limits, with $\chi^2/d.o.f = 1.03$ and a mean gas fraction at 360Kpc of $f_g = 0.11 \pm 0.03$. For

the simulation runs I and III $L_{bX} \simeq 1.3 \cdot 10^{45} \text{ergsec}^{-1}$ and the predicted cluster temperature is $T_X^{\text{pred}} = 5.8 \pm 1.2 \text{eV}$. The error bar represents the 1σ confidence interval. The simulated cluster in the NW run has an emission-weighted temperature $T_X^{\text{em}} = 8.3 \text{KeV}$ and a mass-weighted temperature $T_X^m = 5.6 \text{KeV}$. These values are consistent with those extracted from Figure 5 of YJS for the most massive clusters in their UJ simulations. They are also in good agreement with the values predicted from the mass-temperature relation inferred from cluster *ASCA* and *ROSAT* data (Horner, Mushotzky & Scharf 1999; Nevalainen, Markevitch, & Forman 2000). For the simulation run III the values of L_{bX} and the weighted temperatures are similar to the ones of the NW simulation. Mathiesen & Evrard (2001) have discussed how measurements of the intracluster medium spectral fit temperature T_s are related to T_m and showed that T_s can be considered as a nearly unbiased estimator of T_m . Thus the values of the mass-weighted temperatures reported in Table 6 can be compared with the corresponding T_X^{pred} . The simulations I and III are consistent at the 1σ level with the $L_{bX} - T_X$ relation derived from a sample of cooling flow clusters. Simulations II and IV have $L_{bX} \simeq 4 \cdot 10^{46} \text{ergsec}^{-1}$ and the predicted cluster temperature is outside the 2σ limits.

Another observational test is to compare for the different simulation runs the rates of SF with the observed mean SFR of cluster galaxies. There is now a strong observational evidence that star formation in a cluster environment is strongly suppressed with respect that of field galaxies (Balogh et al. 1998; Poggianti et al. 1999). Kodama & Bower (2000) have estimated the SF histories in rich cluster cores for four clusters, using photometric models constructed from 7 CNOC clusters at $0.23 < z < 0.43$, and found a strong decline in the SF rate relative to the field for $z < 1$. The SF histories of the four clusters are shown in Figure 9 of Kodama & Bower (2000). One of these clusters is Coma, for which the measured values for the mass in galaxies, hot gas and cluster total mass (White et al. 1993) are in the same range as those of the simulated cluster ΛCDM00 . Thus a comparison between the SFR estimated from cluster simulations and the observed data can be made consistently. Although the numerical resolution of the simulations I-III is inadequate to correctly sample the SFR of the galaxies in the cluster, the previous discussion about simulations IH, IIIH and IIIH has shown that even for the low-resolution runs of Table 6, the global cluster SFR is roughly reproduced. Therefore the SF rates computed in simulations I-III can be used for making a crude comparison with the values derived from Kodama & Bower (2000), in order to estimate the consistency of the simulation results for different SF algorithms with observations.

The SF rates plotted in Figure 8 have been estimated by summing the mass of gas converted into stars in time bins of size $\Delta t_s = 3 \cdot 10^7 \text{yr}$. For simulations I and III, at $z = 0$ $\Delta t_s \ll \tau_g$ and the random process used to sample the distribution (3) can be approximated as Poissonian, thus the SFR $\simeq 70 \pm 70 h^{-2} M_\odot \text{yr}^{-1}$; in fact there is only

one single event in the last four time bins. For simulation II, the condition $\Delta t_s \gg \tau_g$ applies and the SFR $\simeq 330 \pm 110 h^{-2} M_\odot yr^{-1}$; the dispersion has been computed over the last four bins. These values must be rescaled to the normalization adopted by Kodama & Bower (2000), who reported the integrated rates for galaxies in the cluster cores in units of $10^{12} M_\odot$ within a radius enclosing 1/3 of the galaxy population. In the simulations of Table 6 $M_s \simeq 1.5 \cdot 10^{13}$ is the total mass in stars, with a small scatter between different runs. Thus $SFR_{(KB)} \simeq 15 \pm 15 h^{-2} M_\odot yr^{-1} / 10^{12} M_\odot$ for simulations I and III, while $SFR_{(KB)} \simeq 66 \pm 22 h^{-2} M_\odot yr^{-1} / 10^{12} M_\odot$ for simulation run II. These values can be compared with $SFR_{(Coma)} \simeq 0.25 h^{-2} M_\odot yr^{-1} / 10^{12} M_\odot$ found by Kodama & Bower (2000) for the Coma cluster at $z \simeq 0.1$. For the cosmology chosen by Kodama & Bower ($\Omega_m = 0.2$ and $h = 0.5$ without a cosmological constant), at this redshift the Coma cluster has an age comparable to that of the simulated clusters at $z = 0$. Therefore simulations I and III have a cluster SFR which is consistent with the observed values. The simulation II, with the KWH method and $c_* = 0.1$, has instead an SFR clearly above the observed limits. For the high resolution runs, the cluster SF rates are above the observed limits for Coma, with simulation IH being marginally consistent at a 2σ level. The Coma cluster has been chosen for comparison because it has a measured cluster SFR and the estimated values for the mass components match those of Λ CDM00. However the Coma cluster does not show a cooling flow activity and the cluster SF rates of the simulations would have been much smaller if Λ CDM00 did not have a cooling instability.

4. Conclusions

In this paper I have analyzed how the gas and X-ray properties of clusters of galaxies estimated from hydrodynamical SPH simulations are affected when radiative cooling is included. It has been found that in order to get reasonable results the inclusion of cooling cannot be decoupled from a prescription for converting cold gas particles into stars. The final results depend on the star formation prescription adopted and the numerical resolution. When the cooling gas particles are converted into stars according to the NW prescription, the final cluster profiles are found to be remarkably stable under changes in the numerical resolution.

This is achieved by using for the individual SPH cluster simulations a number of gas particles $N_g \gtrsim 20,000$ and a gas softening parameter $\varepsilon_g \lesssim 20 h^{-1} Kpc$. Above this numerical threshold, estimates of the final cluster properties can differ among different runs by a factor $\lesssim 2$. It must be stressed that these conclusions are valid for the cluster sample studied here. As discussed in §2, numerical simulations of clusters less massive than those of Table 1

must take into account the metallicity dependence of the cooling function. In this case, the convergence of X-ray variables may require a numerical resolution higher than those considered here.

If the KWH star formation prescription is adopted, with a star formation efficiency parameter $c_\star = 1$, the stability of the final results with respect to the numerical resolution of the simulation is satisfied for the same range of numerical parameters given above for the runs with the NW prescription. The KWH simulations with $c_\star = 0.1$ have been found to give final results which are much more dependent on the simulation numerical resolution. For the KWH runs, the final differences in the gas density profiles at $r \lesssim 100Kpc$ are a consequence of the different SF histories, which depend on c_\star . These differences strongly affect the X-ray luminosity L_X , which is then the simulation variable most sensitive to the value of c_\star . The results demonstrate that, for the same simulated cluster, different SF algorithms yield final gas distributions with differences localized at the cluster center. Global cluster properties, such as the total mass in stars, are robust to different SF prescriptions, while X-ray luminosities can differ by large factors.

A relevant difference for the simulation runs with the NW prescriptions, with respect to previous simulations, is the flatness of the profiles. For the Λ CDM00 cluster the gas profile shows a core radius of $r_c \simeq 20kpc$ and the temperature profile is almost flat for $r \lesssim 100Kpc$. This is at variance with what expected for a cluster with a cooling flow, but the Λ CDM00 cluster has at its center a cooling time $\tau_c(0) \simeq 1/3$ of the universe age $t_U \simeq 13.5Gyr$. The other two clusters which experienced a cooling flow (Λ CDM39 and CHDM39), have $\tau_c(0) \simeq 1Gyr$ and temperature profiles which decline by a factor ~ 2 within the $\sim 200Kpc$ cluster central regions.

A comparison of the temperature profiles with the results of Pearce et al. (2000) and YJS is problematic because these authors adopt a phenomenological prescription for removing cold gas particles from SPH estimates. In the case of YJS the temperature profiles include the cold gas population and show a steep decline at the cluster centers. The profiles of the Cool+SF simulation of Lewis et al. (2000) can be compared with those of the corresponding KWH run with $c_\star = 0.1$ and do not show inconsistencies. Therefore the profiles obtained for the NW run are not inconsistent with previous simulations. The temperature profiles show a decline between the cluster central regions and the virial radii, but the observational evidence for temperature gradients is controversial (Markevitch et al. 1998; Irwin Bregman & Evrard 1999; White 2000).

To summarize, SPH hydrodynamical simulations of clusters of galaxies with radiative cooling and suitable star formation algorithms have been proved to be numerically stable, giving cluster X-ray properties which satisfy a set of observational constraints. An applica-

tion of the numerical schemes adopted to a simulated cluster sample can be used to reliably predict the evolution of the cluster X-ray luminosity and temperature function in different cosmological models. X-ray cluster surveys from the *XMM* mission can then provide strong constraints on the allowed cosmological background parameters, by comparing cluster data with simulation results.

REFERENCES

- Allen, S.W. & Fabian, A.C. 1998a, MNRAS, 297, L57
- Allen, S.W. & Fabian, A.C. 1998b, MNRAS, 297, L63
- Anders, E. & Grevesse, N. 1989, *Geochim. Cosmochim. Acta*, 53, 197
- Anninos, P. & Norman, M.L. 1996, ApJ, 459, 12
- Bahcall, N., Fan, X. & Cen, R. 1997, ApJ, 485, L53
- Bahcall, N.A. & Fan, X. 1998, ApJ, 504, 1
- Balogh, M.L., Schade, D., Morris, S.L., Yee, H.K.C., Carlberg, R.G. & Ellingson, E. 1998, ApJL, 504, L75
- Bryan, G.L., Cen, R., Norman, M.L., Ostriker, J.P. & Stone, J.M. 1994, ApJ, 428, 405
- Bryan, G.R. & Norman, M.L. 1998, ApJ, 495, 80
- Buonomo, F., Carraro, G., Chiosi, C. & Lia, C. 2000, MNRAS, 312, 371
- Buote, D.A., & Tsai, J.C. 1996, ApJ, 458, 27
- Buote, D.A., & Xu, G. 1997, MNRAS, 284, 439
- Buote, D.A. 2000, astro-ph/0001329
- Carraro, G. Lia, C. & Chiosi, C. 1998, MNRAS, 297, 1021
- Cen, R. 1997, ApJ, 485, 39
- Cen R. & Ostriker J., 1994, ApJ, 429, 4
- Cen, R., Kang, H., Ostriker, J.P. & Ryu, D. 1995, ApJ 451, 436
- Crone, M.M., Evrard, A.,E. & Richstone, D.O. 1994, ApJ, 434, 402
- Crone, M.M., Evrard, A.E. & Richstone, D.O. 1996, ApJ, 467, 489
- David, L.P., Slyz, A., Jones, C., Forman, W., Vrtilik, S.D. & Arnaud, K.A. 1993, ApJ, 412, 479
- De Grandi, S. & Molendi, S. 2001, ApJ, 551, 153

- Ebeling, H., Edge, A.C., Fabian, A.C., Allen, S.W., Crawford, C.S. & Boehringer, H. 1997, ApJ, 479, L1
- Ebeling, H., Edge, A.C., Bohringer, H., Allen, S.W., Crawford, C.S., Fabian, A.C., Voges, W. & Huchra, J.P. 1998, MNRAS, 301, 881
- Edge, A.C., Stewart, G.C., Fabian, A.C. & Arnaud, K.A. 1990, MNRAS, 245, 559
- Eke, V.R., Cole, S. & Frenk, C.S. 1996, MNRAS, 282, 263
- Eke, V.R., Cole, S., Frenk, C.S. & Henry, J.P. 1998, MNRAS, 298, 1145
- Eke, V.R., Navarro, J.F. & Frenk, C.S. 1998, ApJ, 503, 569
- Evrard, A.E. 1988, MNRAS, 235, 911
- Evrard, A.E. 1990, ApJ, 363, 349
- Evrard, A.E. 1997, MNRAS, 292, 289
- Evrard, A.E. & Henry, J.P. 1991, ApJ, 383, 95
- Ezawa, H., Fukazawa, Y., Makishima, K., Ohashi, T. Takahara, F., Xu, H. & Yamasaki, N.Y. 1997, ApJL, 490, 33
- Fabian, A.C. 1994, ARAA, 32, 277
- Fabian, A.C., Crawford, C.S., Edge, A.C. & Mushotzky, R.F. 1994, MNRAS, 267, 779
- Farouki, R.T. & Salpeter, E.E. 1982, ApJ, 253, 512
- Frenk, C.S. et al. 1999, ApJ, 525, 554
- Forman W. & Jones, C. 1982, ARAA, 20, 547
- Fukazawa, Y. et al. 1998, PASJ, 50, 187
- Gingold, R.A. & Monaghan, J.J. 1977, MNRAS, 181, 375
- Girardi, M., Borgani, S., Giuricin, G., Mardirossian, F. & Mezzetti, M. 1998, ApJ, 506, 45
- Henry, J.P. & Arnaud, K.A. 1991, ApJ, 372, 410
- Henry, J.P., Gioia I.M., Maccacaro T., Morris S.L., Stocke J.T. & Wolter A. 1992, ApJ, 386, 408

- Henry, J.P. 1997, ApJ, 489, L1
- Hernquist, L. 1987, ApJS, 64, 715
- Hernquist, L. & Katz, N. 1989, ApJS, 70, 419
- Horner, D.J., Mushotzky, R.F. & Scharf, C. 1999, ApJ, 520, 78
- Huss, A., Jain, B. & Steinmetz, M. 1999, MNRAS, 308, 101
- Irwin, J.A., Bregman, J.N. & Evrard, A.E. 1999, ApJ, 519, 518
- Jing, Y.P., Mo, H.J., Börner, G., Fang, L.Z. 1995, MNRAS, 276, 417
- Jing, Y.P. & Suto, Y., 2000, astro-ph/0001288
- Kaiser N. 1986, MNRAS, 222, 323
- Kang, H. , Cen, R. , Ostriker, J.P. & Ryu, D. 1994, ApJ, 428, 1
- Katz, N. 1992, ApJ, 391, 502
- Katz, N. & White, S.D.M. 1993, ApJ, 412, 455
- Katz, N., Weinberg, D.H. & Hernquist, L. 1996, ApJS, 105, 19
- Kikuchi, K., Furusho, T., Ezawa, H., Yamasaki, N.Y., Ohashi, T., Fukazawa, Y. & Ikebe, Y. 1999, PASJ, 51, 301
- Kitayama, T. & Suto, Y. 1996, ApJ, 469, 480
- Kitayama, T., Sasaki, S. & Suto, Y. 1998, PASJ, 50, 1
- Kodama, T. & Bower, R.G. 2000, astro-ph/0005397
- Lacey, C. & Cole, S. 1994, MNRAS, 271, 676
- Lia, C. & Carraro, G. 2000, MNRAS, 314, 145
- Lia, C., Carraro, G. & Salucci, P. 2000, astro-ph/0006012
- Lilje, P.B. 1992, ApJ, 386, L33
- Lewis, G.F., Babul, A., Katz, N., Quinn, T., Hernquist, L. & Weinberg, D.H. 2000, ApJ , 536, 623
- Makino, N., Sasaki, S., Suto, Y. 1998, ApJ, 497, 555

- Markevitch, M. 1998, ApJ, 504, 27
- Markevitch, M., Forman, W.R., Sarazin, C.L. & Vikhlinin, A. 1998, ApJ, 503, 77
- Mathiesen, B. & Evrard, A.E. 1998, MNRAS, 295, 769
- Mathiesen, B. & Evrard, A.E. 2001, ApJ, 546, 100
- Miller, G.E. & Scalo, F.J.M. 1979, ApJS, 41, 513
- Monaghan, J.J. 1992, ARAA, 30, 543
- Moore, B., Governato, F., Quinn, T., Stadel, J. & Lake, G. 1998, ApJL, 499, 5
- Navarro, J. & White, S.D.M. 1993, MNRAS, 265, 271 (NW)
- Navarro, J., Frenk C.S. & White, S.D.M. 1995, MNRAS, 275, 720
- Navarro, J., Frenk C.S. & White, S.D.M. 1997, ApJ, 490, 493
- Nevalainen, J., Markevitch, M. & Forman, W. 2000, ApJ 532, 694
- Oukbir, J. & Blanchard, A. 1992, AA, 262, L21
- Pearce, F.R., Thomas, P.A., Couchman, H.M.P. & Edge, A.C. 2000, MNRAS 317, 1029
- Peebles, P.J.E., Daly, R.A. & Juskiewicz, R. 1989, ApJ, 347, 563
- Peres, C.B., Fabian, A.C., Edge, A.C., Allen, S.W., Johnstone, R.M. & White, D.A. 1998, MNRAS, 298, 416
- Poggianti, B.M., Smail, I., Dressler, A., Couch, W.J., Barger, A.J., Butcher, H.E., Richard, S. & Oemler, A.Jr. 1999, ApJ, 518, 576
- Ponman, T.J., Cannon, D.B. & Navarro, J.F. 1999, Nature, 397, 135
- Press, W.H. & Schechter, P. 1974, ApJ, 187, 425
- Rosati, P., Della Ceca, R., Norman, C. & Giacconi, R. 1998, ApJ, 492, L21
- Sadat R., Blanchard, A. & Oukbir, J. 1998, AA, 329, 21
- Sarazin, C.L. 1986, Reviews of Modern Physics, 58, 1
- Steinmetz, M. & Mueller, E. 1994, AA, 281, L97
- Steinmetz, M. & White, S.D.M. 1997, MNRAS, 288, 545

- Suginohara, T. & Ostriker, J.P. 1998, *ApJ*, 507, 16
- Tantalo, R., Chiosi, C. & Bressan A. 1998, *AA*, 333, 419
- Thacker, R.J., Tittley, E.R., Pearce, F.R., Couchman, H.M.P. & Thomas, P.A. 2000, *MNRAS*, 319, 619
- Thacker, R.J. & Couchman, H.M.P. 2000, *ApJ*, 545, 728
- Thomas, P.A. & Couchman, H.M.P. 1992, *MNRAS*, 257, 11
- Thomas, P.A., Fabian, A.C. & Nulsen, P.J.E. 1987, *MNRAS*, 228, 973
- Valdarnini, R., Ghizzardi, S. & Bonometto, S. 1999, *New Astr*, 4, 71 (VGB)
- Viana, P.T.P. & Liddle, A.R. 1999, *MNRAS*, 303, 535
- West, M.J., Oemler, A.J. & Dekel, A. 1998, *ApJ*, 327, 1
- White, D.A. 2000, *MNRAS*, 312, 663
- White, S.D.M., Navarro, J.F, Evrard, A.E. & Frenk C.S. 1993, *Nature*, 366, 426
- White, S.D.M., Efstathiou, G. & Frenk, C.S. 1993, *MNRAS*, 262, 1023
- Wu, K.K.S., Fabian, A.C. & Nulsen, P.E.J. 1998, *MNRAS*, 301, L20
- Yoshikawa, K., Itoh, M. & Suto, Y. 1998, *PASJ*, 50, 203
- Yoshikawa, K., Jing, Y.P. & Suto, Y. 2000, *ApJ*, 535, 593 (YJS)

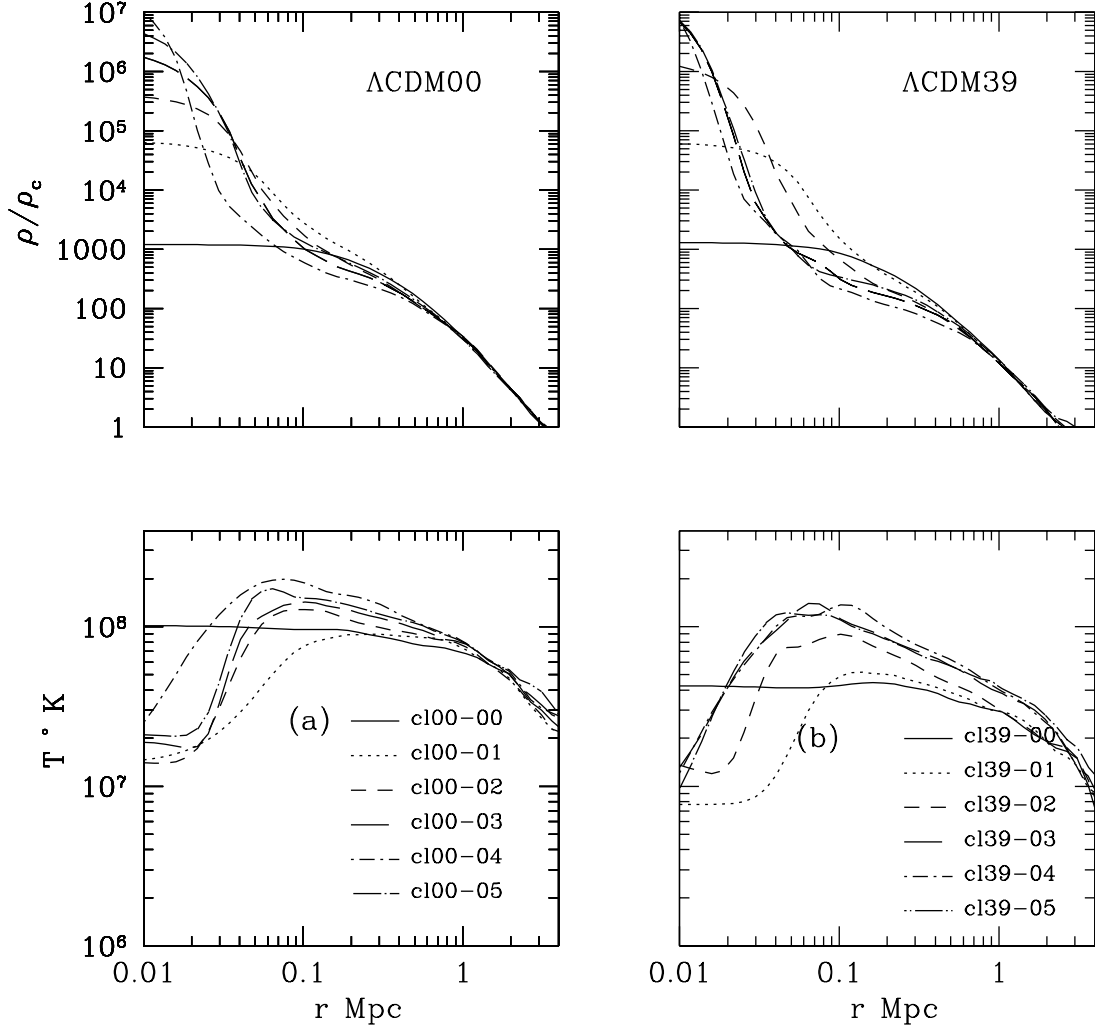


Fig. 1.— Radial dependence of the gas density and temperature profile at $z = 0$ in simulations with radiative cooling. The left panel is for the test cluster Λ CDM00, the right panel for Λ CDM39. In each panel, the upper plot is for densities and the lower plot is for gas temperatures. The density is in units of the critical density. The different curves are for integrations with different numbers of particles and different softening parameters (see Tables 2 & 3). The simulation run with index -00 is the integration without cooling.

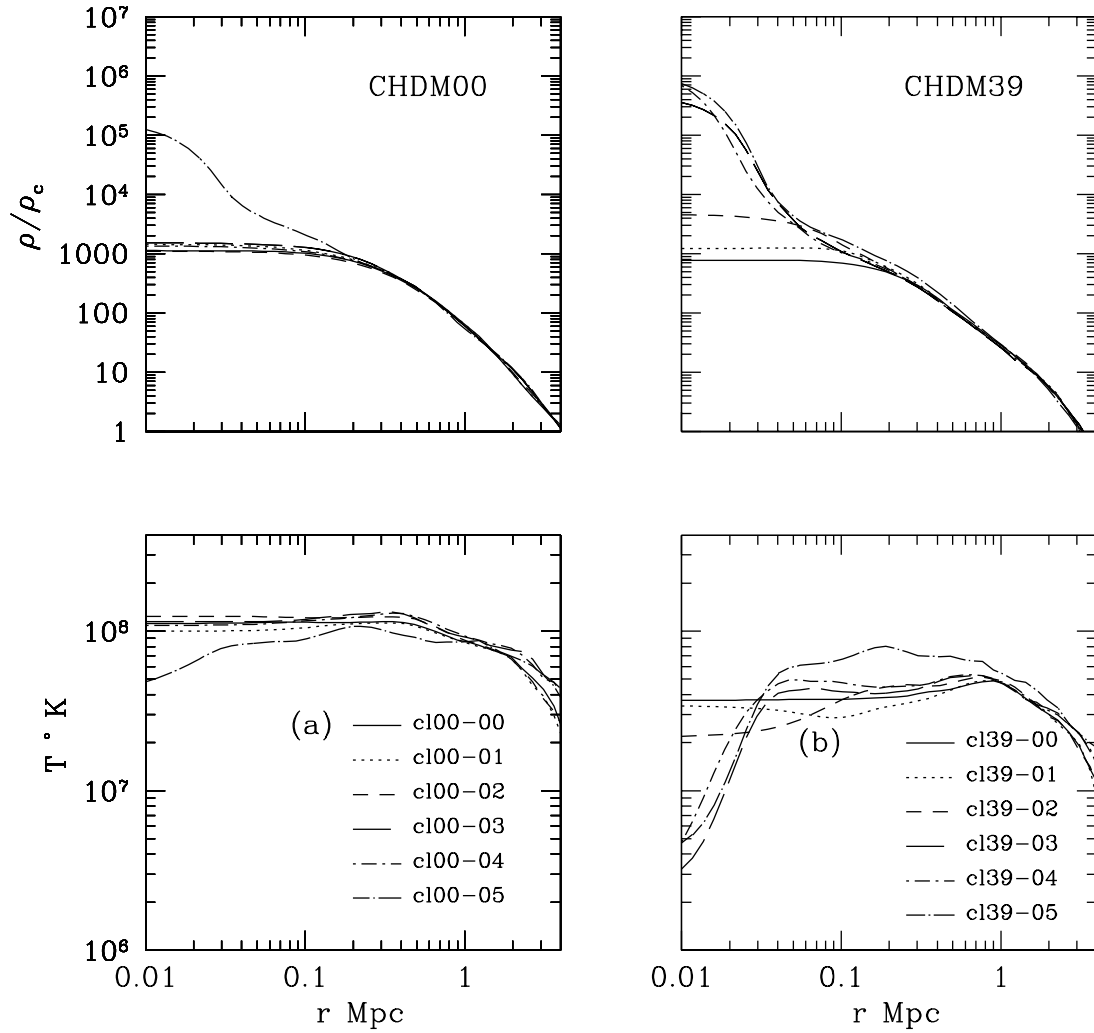


Fig. 2.— As in Fig. 1, but for the test clusters CHDM00 and CHDM39. The numerical parameters of the simulations are given in Tables 4 and 5.

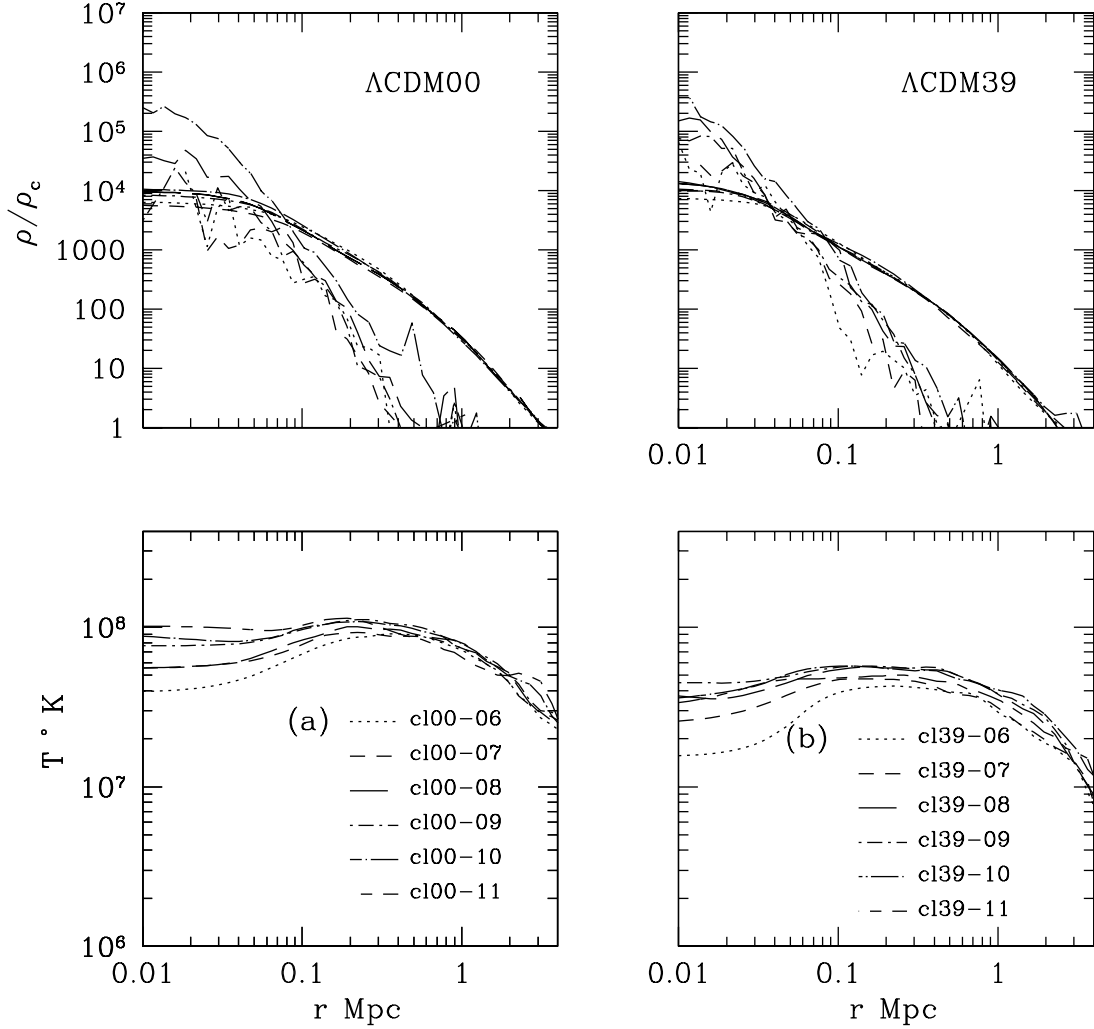


Fig. 3.— Final density and temperature profiles for the simulation runs including radiative cooling and star formation. The gas is allowed to convert into stars according to the NW star formation prescription (see text). The simulations are the same shown in Fig. 1, with the numerical parameters reported in Tables 3 & 5. The index of the simulations is $cl00 - k$ or $cl39 - k$, with $k = j + 5$ and $j = 1, 5$ is the index of the cooling runs in Tables 2 & 5. The simulations with index $k = 11$ have the same parameters as the $k = 10$ runs, but with the gravitational tolerance parameter $\theta = 1$ and quadrupole corrections enabled. The other simulations were performed with $\theta = 0.7$ without quadrupole corrections. In the density plots, the lines with a steeper slope ($\simeq -3$) show the density behavior of the star component.

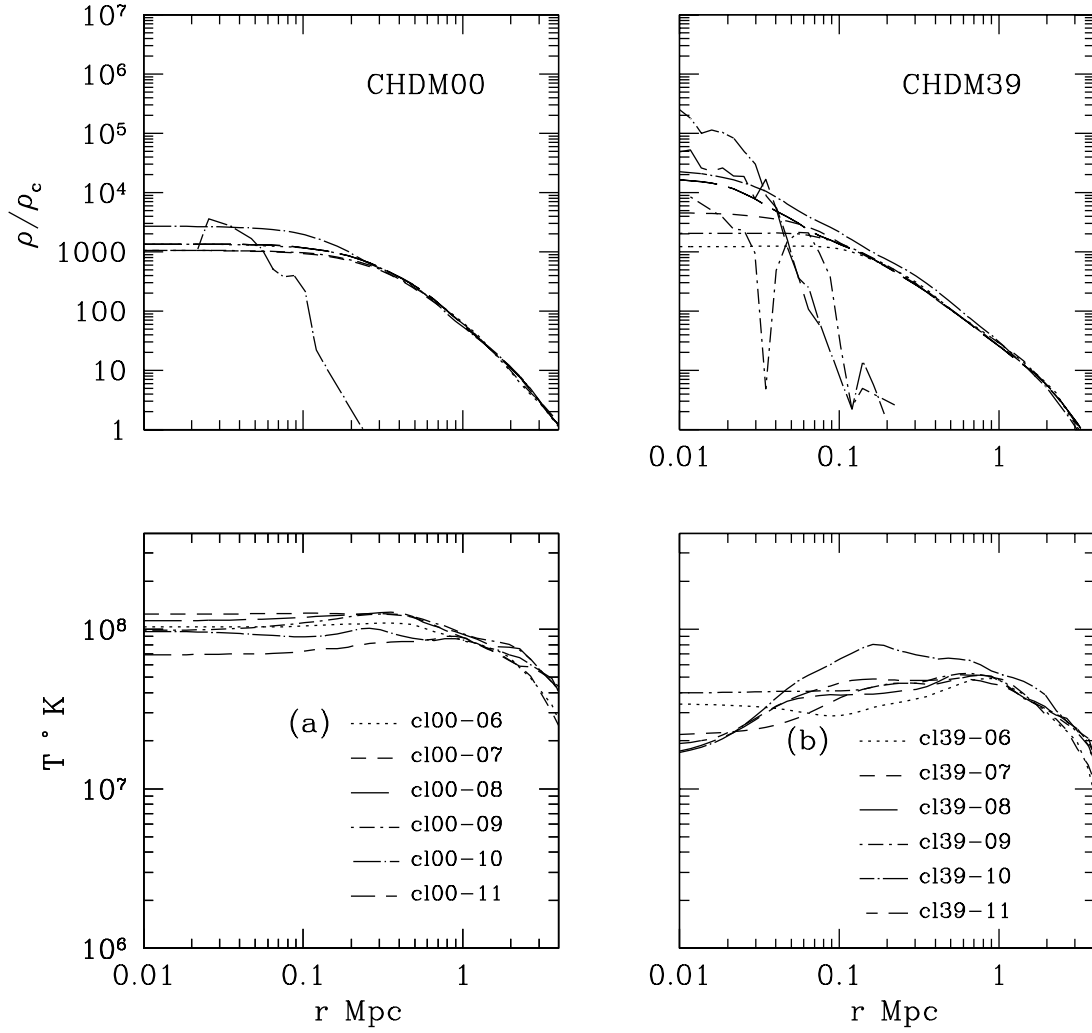


Fig. 4.— As in Fig. 3, but for the cluster simulations shown in Fig. 2.

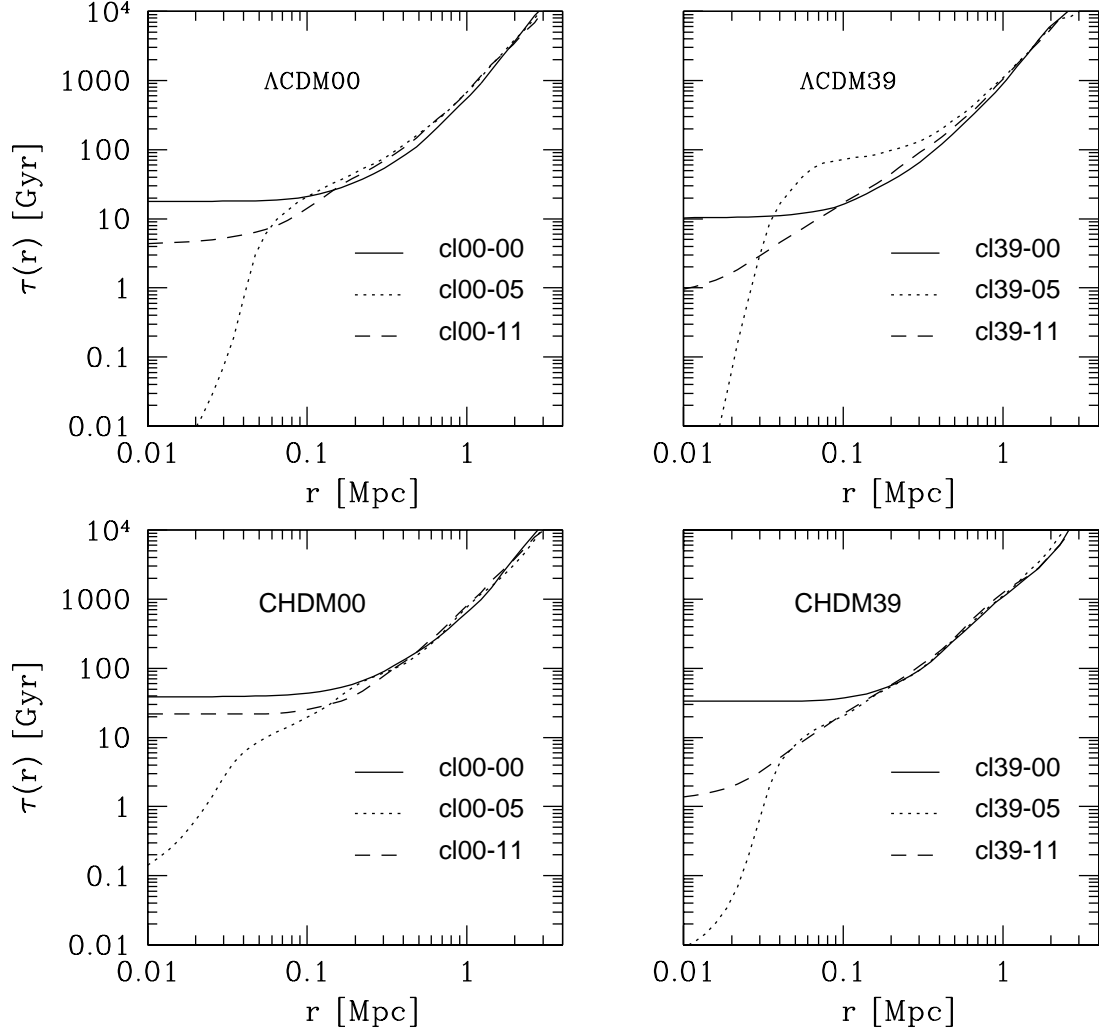


Fig. 5.— The cooling time τ_c as a function of radial distance for the four test clusters. τ_c is defined according to equation 6. In each panel, τ_c is plotted for three different tests; the continuous line is the case with no cooling, the dotted line is the pure cooling test simulation with the highest resolution (-05), the short-dashed line is the equivalent simulation run but with gas particles being allowed to undergo star formation.

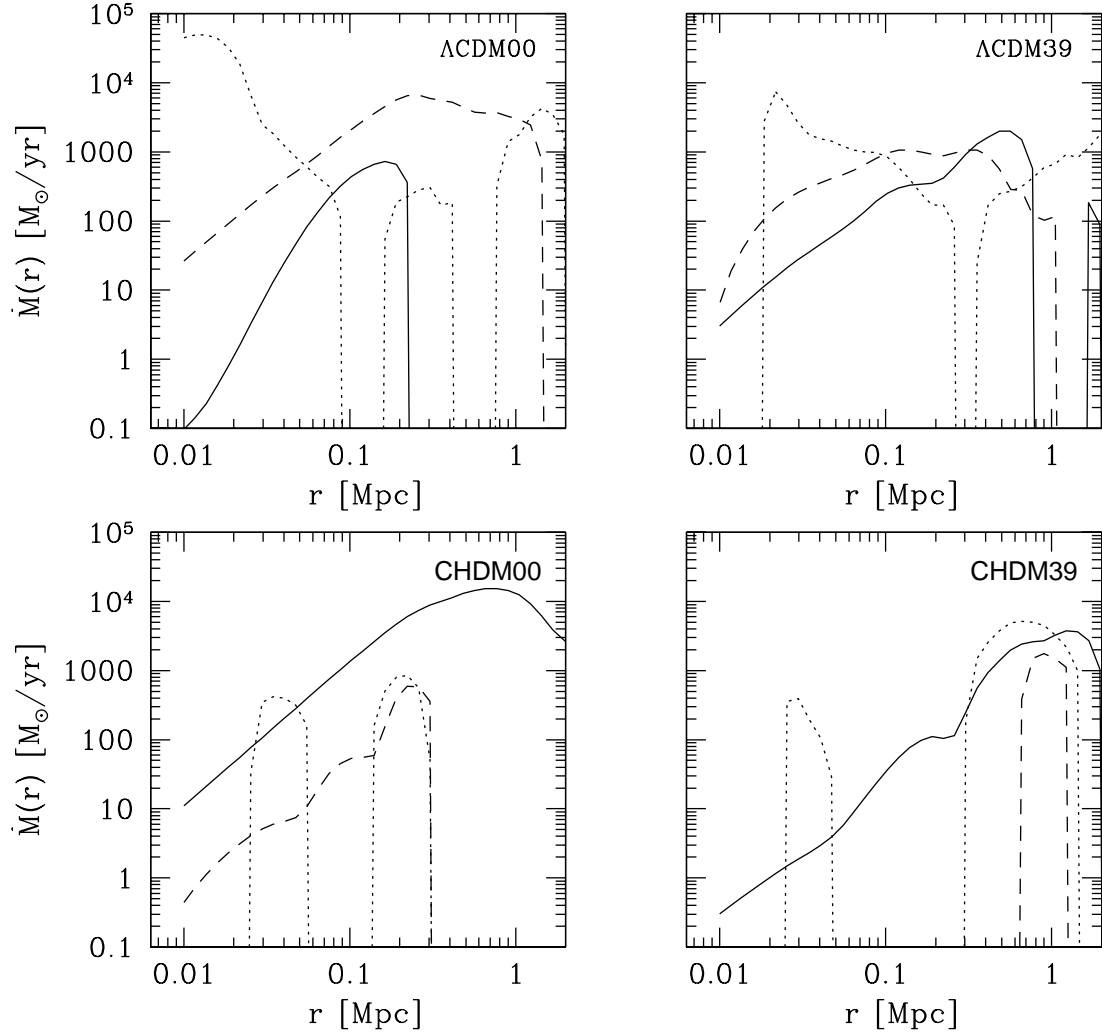


Fig. 6.— Mass accretion rates in the four test clusters for the same simulation tests shown in Fig. 5. In each radial bin, spherical averages for $\dot{M}(r) = 4\pi\rho_g r^2 v_r$ have been plotted only for negative values of the radial infall velocity v_r .

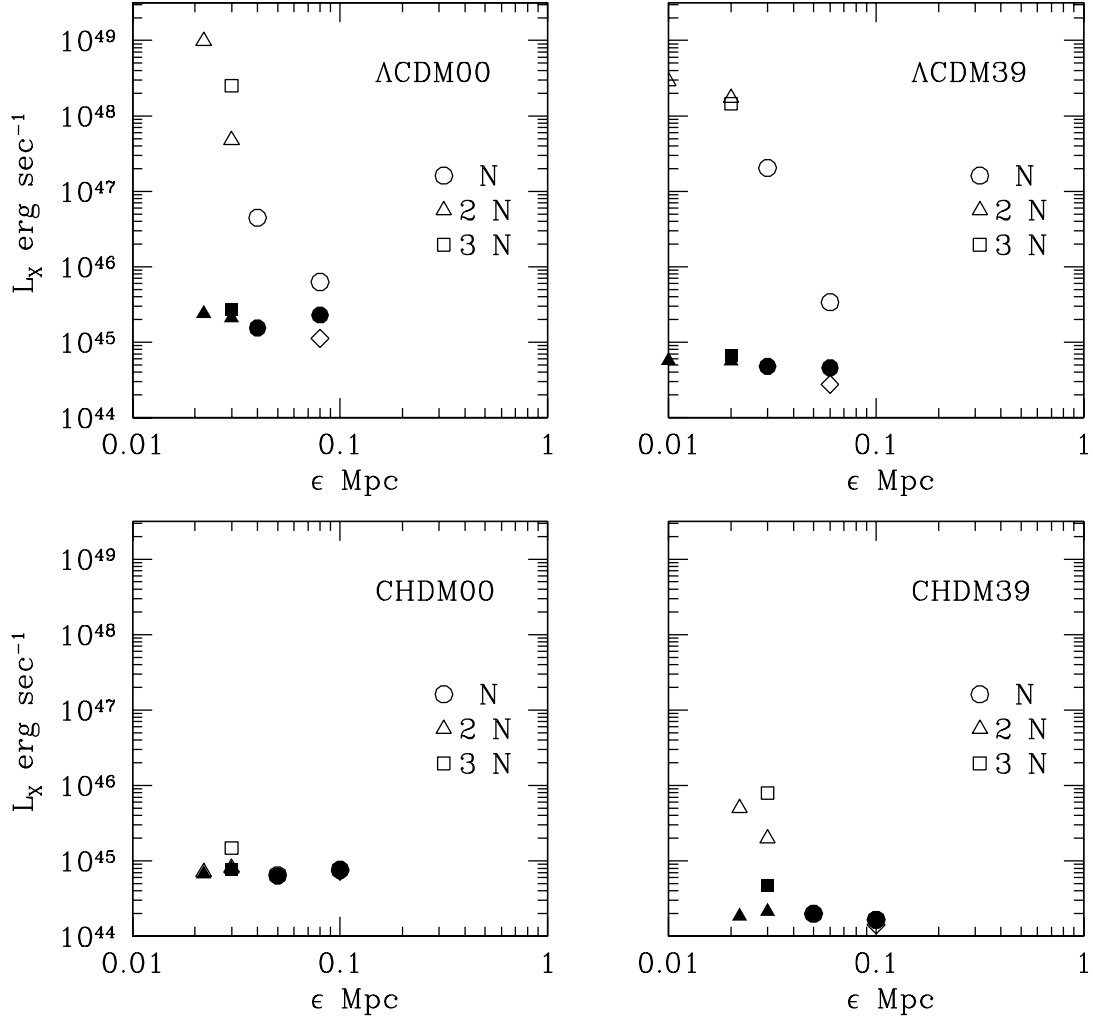


Fig. 7.— Final cluster X-ray luminosities as a function of ϵ_g for the simulation runs performed for the four test clusters. In each panel L_X is shown for the simulations with gas cooling (open symbols) and for those also including star formation (filled symbols). For these test runs, values of the numerical inputs are reported in Tables 2, 3, 4 & 5. Simulation clusters with index cl00 – j or cl39 – j correspond to the following symbols: diamond $j = 00$; circle $j = 01, 02$; triangle $j = 03, 04$; square $j = 05$. The filled symbols are the simulations with index $j + 5$.

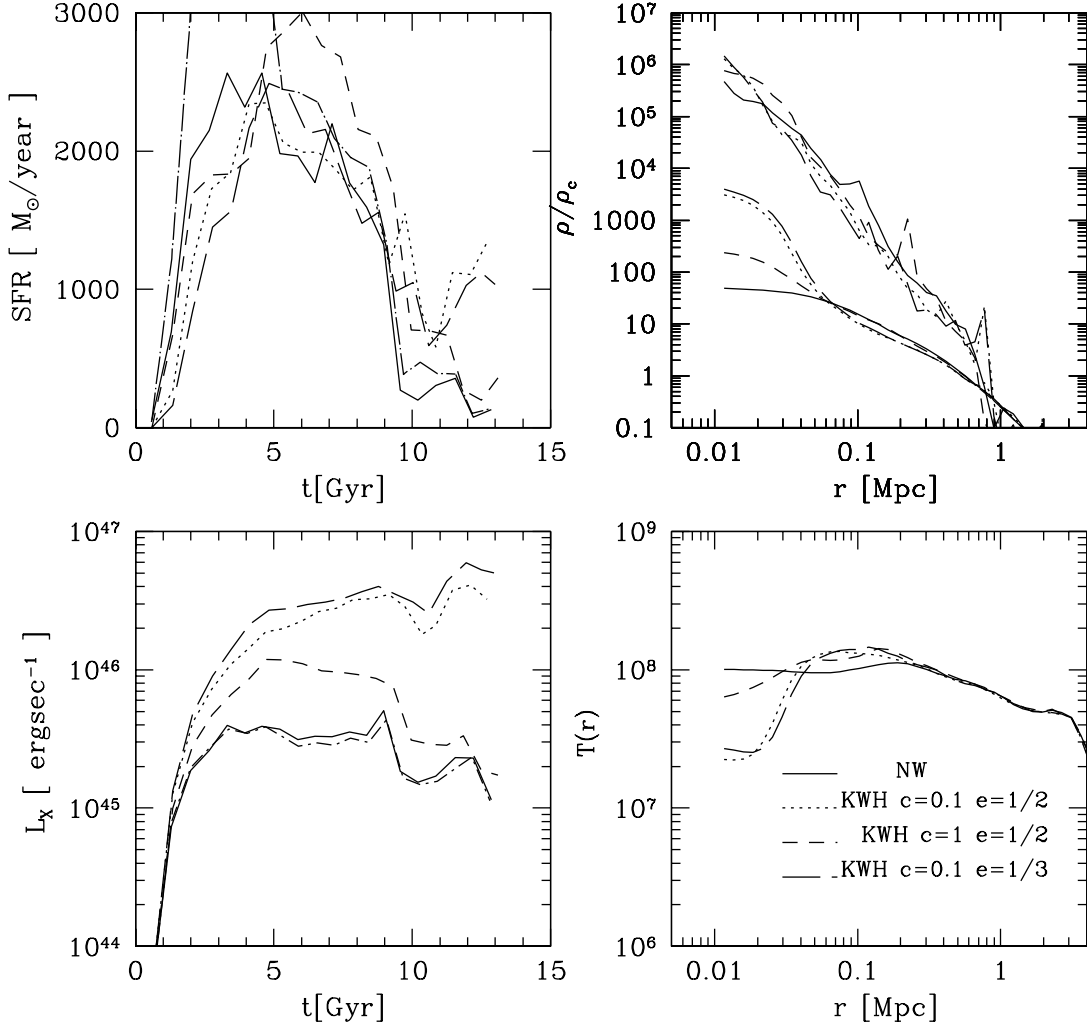


Fig. 8.— Plots showing several cluster properties in simulation runs for the same cluster, but with different SF prescriptions. The test cluster is Λ CDM00, and the simulation parameters are those of cl00 – 11 (see Table 3). The different curves are for different SF methods or parameters, as reported in Table 6. The continuous line refers to the NW method, the others to KWH with different c_* and ε_* (c and e in the bottom right panel). *Top left*: star formation rate as a function of time. *Bottom left*: X-ray luminosity versus time. *Top right*: final radial density behavior for the gas and star components; for the sake of clarity the gas densities have been shifted downwards by a factor of 100. *Bottom right*: Radial temperature profiles. The dot-dashed line in the two left panels is for a simulation run with the NW method, but with an SN explosion energy of $\varepsilon_{SN} = 10^{50} \text{erg}$.

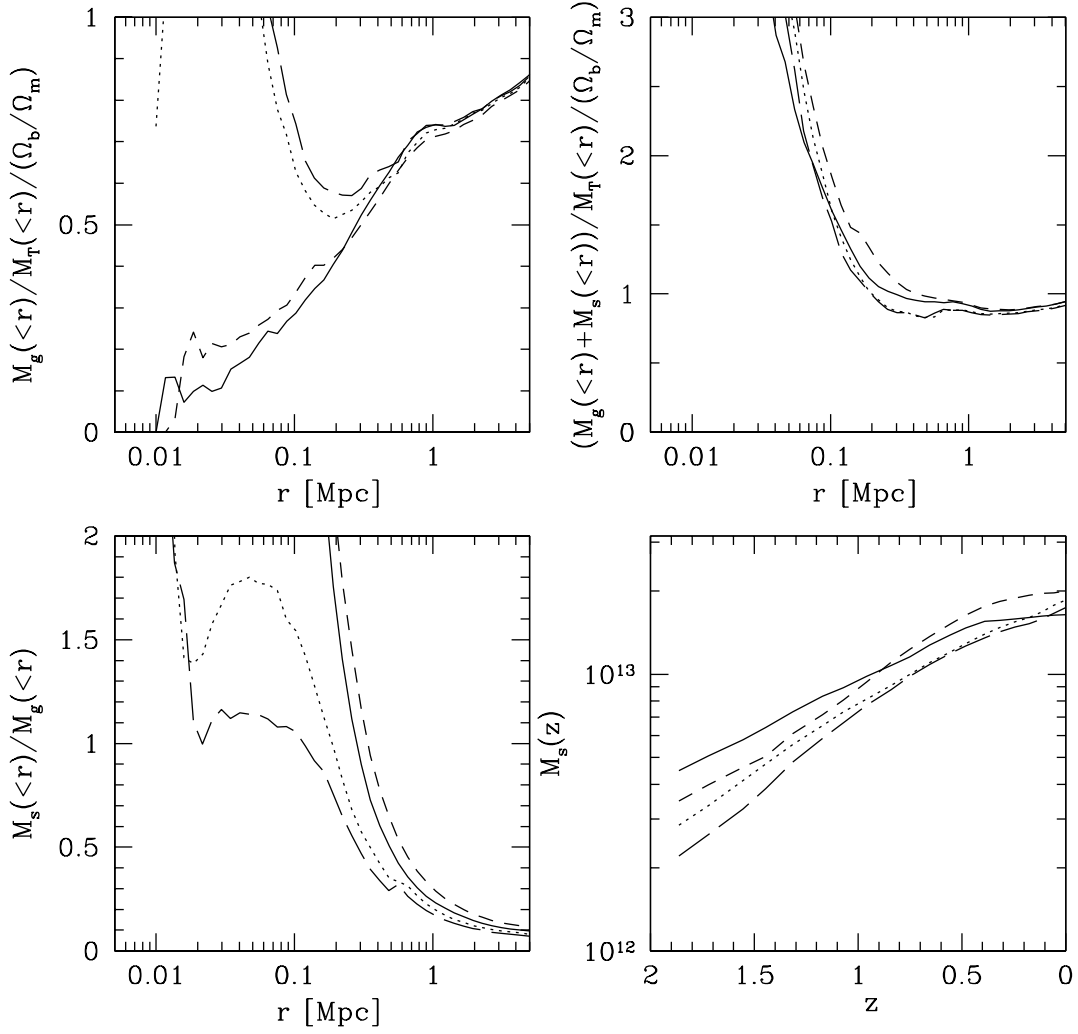


Fig. 9.— Baryonic fractions versus radius for the same simulations shown in Fig. 8. *Top left:* ratio of the total mass of gas within the radius r , to the cumulative cluster mass in units of the universal baryonic fraction. *Top right:* as in the left panel but for the ratio of (star+gas) mass to the total cluster mass. *Bottom left:* ratio of the star mass within radius r to the mass of gas within r . *Bottom right:* total mass produced in stars as a function of redshift.

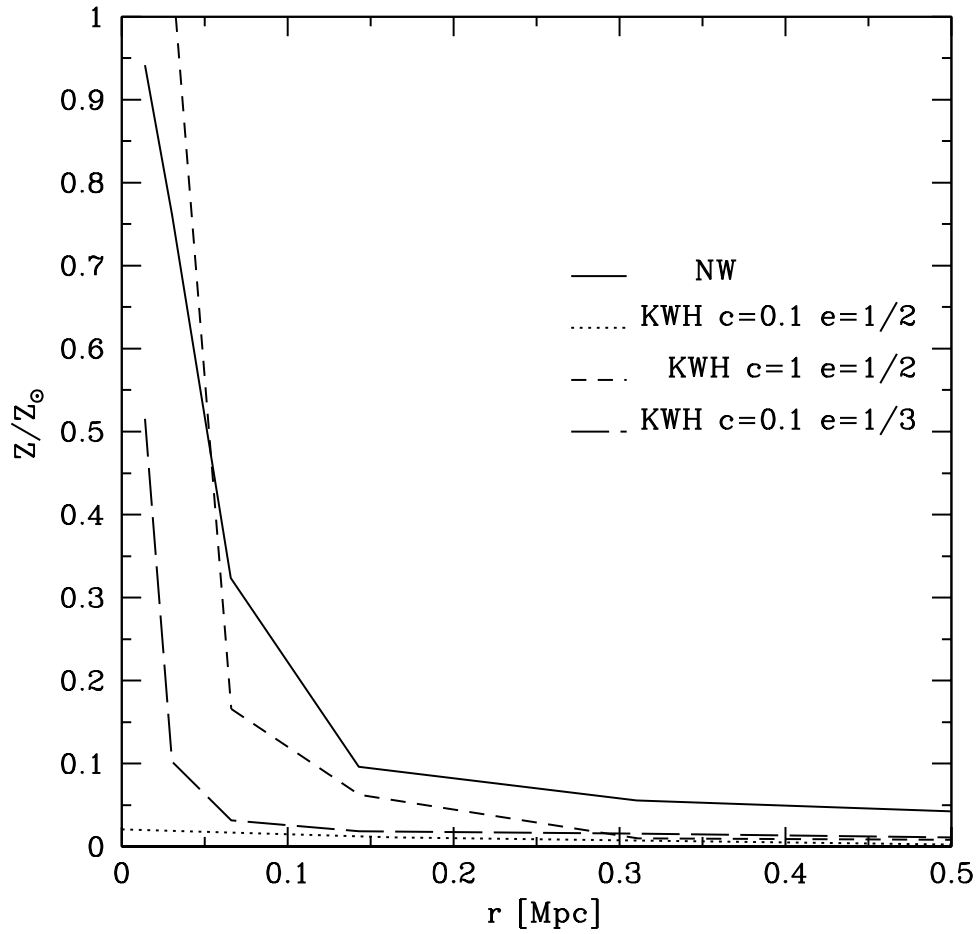


Fig. 10.— Spherically averaged iron abundances $Z = Fe/H$ as a function of radius at the final epoch in units of the solar value $4.68 \cdot 10^{-5}$. The different lines correspond to the simulations of Fig. 8.

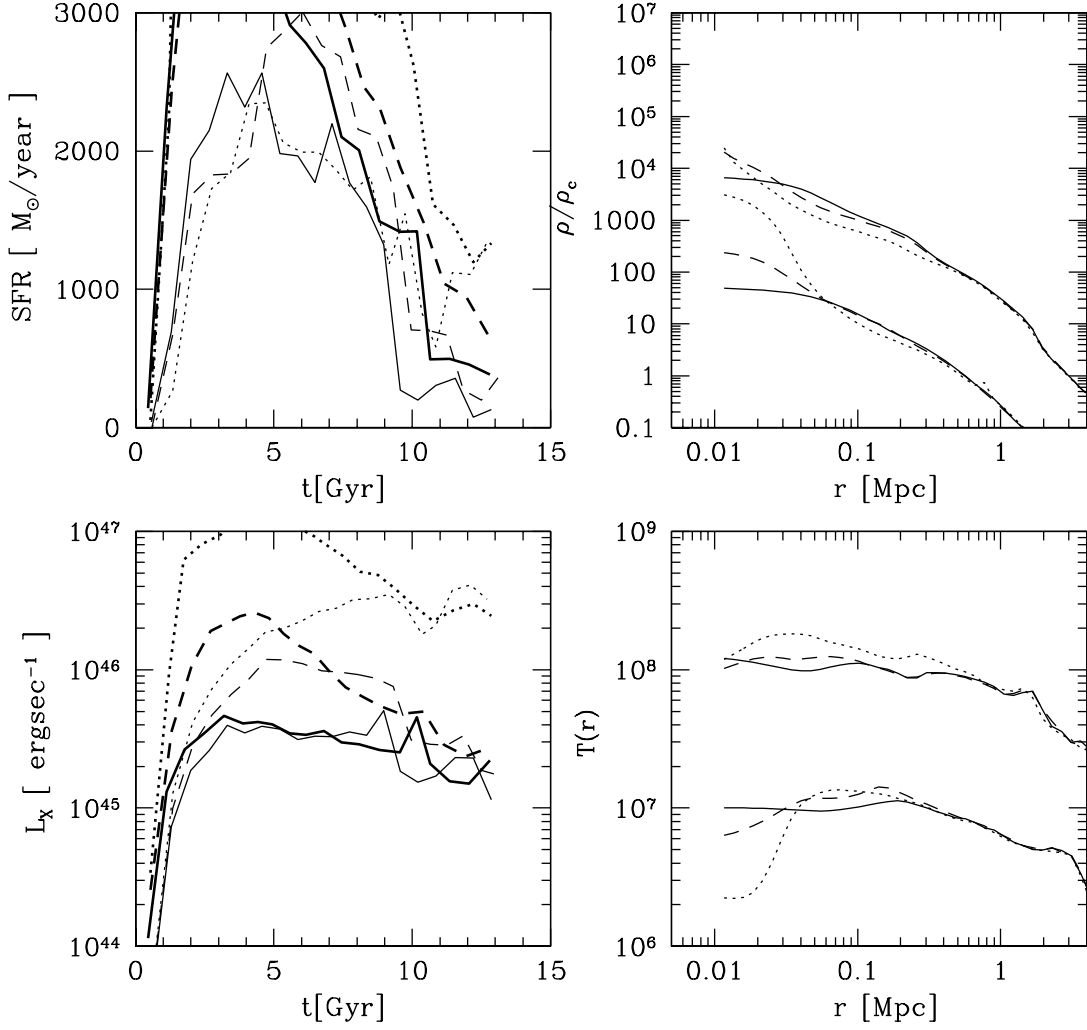


Fig. 11.— For the first three runs I, II, III of Table 6, the simulation results of Fig. 8 are compared with the corresponding high-resolution runs IH, IIH and IIIH. The H simulations have the same SF parameters as the parent simulations, but the numerical parameters are given in the last row of Table 3. *Left panels*: the thick lines correspond to the high resolution simulations. *Right panels*: to facilitate a comparison with the high resolution results, the radial profiles of Fig. 8 have been shifted downwards by 10^k , $k = 2$ for densities and $k = 1$ for temperatures.

Table 1. Properties of the simulated clusters

cluster	M_{200}	r_{200}	σ_1
CHDM00	$1.4 \cdot 10^{15}$	1.83	1500
CHDM39	$4.4 \cdot 10^{14}$	1.25	1000
Λ CDM00	$1.2 \cdot 10^{15}$	1.98	1200
Λ CDM39	$4 \cdot 10^{14}$	1.37	800

Note. — Reference values at $z = 0$ for the four clusters used in the numerical tests. M_{200} : cluster mass within r_{200} in units of $h^{-1}M_{\odot}$, r_{200} is in units of h^{-1} Mpc, σ_1 is the central 1-D dark matter velocity dispersion in $Kmsec^{-1}$. M_{200} is defined as $M_{200} = (4\pi/3)\Omega_m\rho_c\Delta_c r_{200}^3$, with $\Delta_c = 187\Omega_m^{-0.55}$ for a flat cosmology.

Table 2. Numerical parameters of the simulations with cooling for the Λ CDM00 cluster

Λ CDM00	ε_g^a	m_g^b	m_d^c	N_g^d	N_d^e	N_T^f	θ^g	Q^h	z_{in}^i
cl00-00	56	$3.01 \cdot 10^{10}$	$2.64 \cdot 10^{11}$	5503	6295	16463	0.7	F	10.
cl00-01	56	$3.01 \cdot 10^{10}$	$2.64 \cdot 10^{11}$	5503	6295	16463	0.7	F	10.
cl00-02	28	$3.01 \cdot 10^{10}$	$2.64 \cdot 10^{11}$	5503	6295	16463	0.7	F	10.
cl00-03	21	$1.45 \cdot 10^{10}$	$1.28 \cdot 10^{11}$	11480	14208	35408	0.7	F	10.
cl00-04	15.4	$1.45 \cdot 10^{10}$	$1.28 \cdot 10^{11}$	11480	14208	35408	0.7	F	10.
cl00-05	21	$7.47 \cdot 10^9$	$6.57 \cdot 10^{10}$	22575	25391	67388	0.7	F	19.

Note. — Simulation parameters of the five test runs for the Λ CDM00 cluster. cl00 – 00 is the reference case with no cooling, taken from VGB. a : gravitational softening parameter for the gas in h^{-1} Kpc. b : mass of the gas particles in $h^{-1}M_\odot$ (the cosmology is for $\Omega_m = 0.3$ and $h = 0.7$). c : mass of the dark particles. d : number of gas particles inside the $L_c/2$ sphere at $z = z_{in}$. e : as in the previous column but for dark particles. f : total number of simulation particles, including those in the external shell of radius L_c . g : value of the treecode gravitational tolerance parameter. h : gravitational quadrupole corrections $F =$ disabled, $T =$ enabled. i : initial redshift for the simulation.

Table 3. Numerical parameters for the simulations with cooling and star formation for the Λ CDM00 cluster

Λ CDM00	ε_g	m_g	m_d	N_g	N_d	N_T	θ	Q	z_{in}
cl00-06	56	$3.01 \cdot 10^{10}$	$2.64 \cdot 10^{11}$	5503	6295	16463	0.7	F	10.
cl00-07	28	$3.01 \cdot 10^{10}$	$2.64 \cdot 10^{11}$	5503	6295	16463	0.7	F	10.
cl00-08	21	$1.45 \cdot 10^{10}$	$1.28 \cdot 10^{11}$	11480	14208	35408	0.7	F	10.
cl00-09	15.4	$1.45 \cdot 10^{10}$	$1.28 \cdot 10^{11}$	11480	14208	35408	0.7	F	10.
cl00-10	21	$7.47 \cdot 10^9$	$6.57 \cdot 10^{10}$	22575	25391	67388	0.7	F	19.
cl00-11	21	$7.47 \cdot 10^9$	$6.57 \cdot 10^{10}$	22575	25391	67388	1.0	T	19.
cl00-11H	10.5	$2.45 \cdot 10^9$	$2.12 \cdot 10^{10}$	69599	74983	204799	1.0	T	29.

Note. — As in Table 2, simulation parameters of the test runs including cooling and star formation for the Λ CDM00 cluster. The index of the run is cl00- k , with $k = j + 5$ and $j = 1, 5$ is the index of the cooling simulation. The numerical parameters of the cooling and star formation runs are those of the corresponding cooling simulation with index j . The last row gives the numerical parameters for the high-resolution runs used to test different SF methods.

Table 4. CHDM00

CHDM00	ε_g	m_g	m_d^a	N_g	N_d^a	N_T	z_{in}
cl00-00	50	$2.28 \cdot 10^{10}$	$3.57 \cdot 10^{11}$	5551	13038	27971	4.8
cl00-01	50	$2.28 \cdot 10^{10}$	$3.57 \cdot 10^{11}$	5551	13038	27971	4.8
cl00-02	25	$2.28 \cdot 10^{10}$	$3.57 \cdot 10^{11}$	5551	13038	27971	4.8
cl00-03	15	$1.1 \cdot 10^{10}$	$1.73 \cdot 10^{11}$	11507	29038	59093	4.8
cl00-04	11	$1.1 \cdot 10^{10}$	$1.73 \cdot 10^{11}$	11507	29038	59093	4.8
cl00-05	15	$5.5 \cdot 10^9$	$8.9 \cdot 10^{10}$	22575	50726	112512	9

Note. — As in Table 2, but for CHDM00. ^a : m_d and N_d are the total cold+hot values.

Table 5. Λ CDM39 and CHDM39

	Λ CDM39			CHDM39		
	ε_g	m_g	m_d	ε_g	m_g	m_d
cl39-00	42	$1.47 \cdot 10^{10}$	$1.3 \cdot 10^{11}$	50	$7.5 \cdot 10^9$	$1.19 \cdot 10^{11}$
cl39-01	42	$1.47 \cdot 10^{10}$	$1.3 \cdot 10^{11}$	50	$7.5 \cdot 10^9$	$1.19 \cdot 10^{11}$
cl39-02	21	$1.47 \cdot 10^{10}$	$1.3 \cdot 10^{11}$	25	$7.5 \cdot 10^9$	$1.19 \cdot 10^{11}$
cl39-03	14	$7.2 \cdot 10^9$	$6.37 \cdot 10^{10}$	15	$3.7 \cdot 10^9$	$5.75 \cdot 10^{10}$
cl39-04	10.5	$7.2 \cdot 10^9$	$6.37 \cdot 10^{10}$	11	$3.7 \cdot 10^9$	$5.75 \cdot 10^{10}$
cl39-05	14	$3.7 \cdot 10^9$	$3.22 \cdot 10^{10}$	15	$1.89 \cdot 10^9$	$2.96 \cdot 10^{10}$

Note. — Simulation parameters of the test runs for the clusters Λ CDM39 and CHDM39. The number of particles and initial redshifts are the same as for the 00 clusters.

Table 6. Simulation runs with different star formations parameters

method	c_*	ε_*	ε_{SN}	T_{em}^a	T_m^b	$T_{em}^c (< 50Kpc)/T_{em}$	run
NW	1	1/2	1	8.3	5.66	0.08	I
KWH	0.1	1/2	1	1.9	5.5	0.8	II
KWH	1	1/2	1	8.96	5.77	0.2	III
KWH	0.1	1/3	1	2.05	5.42	0.87	IV
NW	1	1/2	0.1	7.88	5.54	0.08	V

Note. — SF parameters for the simulations used to compare different models of SF. The test cluster is Λ CDM00 and the numerical parameters are those of cl00 – 11 (see Table 3). The different SF parameters are defined in §2, ε_{SN} is the SN explosion energy in units of $10^{51}erg$. a : emission weighted temperature in KeV units at $z = 0$. b : mass-weighted temperature at $z = 0$. c :relative contribution to the total emission-weighted temperature from the $r = 50Kpc$ cluster inner region.